

#### **PAPER • OPEN ACCESS**

# Plasma–surface interaction in the stellarator W7-X: conclusions drawn from operation with graphite plasma-facing components

To cite this article: S. Breznsek et al 2022 Nucl. Fusion 62 016006

View the article online for updates and enhancements.

#### You may also like

- <u>Wall conditioning at the Wendelstein 7-X</u> <u>stellarator operating with a graphite</u> divertor
- A Goriaev, T Wauters, R Brakel et al.
- Inspection of W 7-X plasma-facing components after the operation phase OP1.2b: observations and first assessments
- C P Dhard, S Äkäslompolo, M Balden et al.
- Measurement and modeling of magnetic configurations to mimic overload scenarios in the W7-X stellarator J.D. Lore, Y. Gao, J. Geiger et al.

Nucl. Fusion 62 (2022) 016006 (23pp)

# Plasma-surface interaction in the stellarator W7-X: conclusions drawn from operation with graphite plasma-facing components

```
S. Brezınsek<sup>1,*</sup>, C.P. Dhard<sup>2</sup>, M. Jakubowski<sup>2</sup>, R. König<sup>2</sup>, S. Masuzaki<sup>3</sup>, M. Mayer<sup>4</sup>, D. Naujoks<sup>2</sup>, J. Romazanov<sup>1,5</sup>, K. Schmid<sup>4</sup>, O. Schmitz<sup>6</sup>, D. Zhao<sup>1,7</sup>, M. Balden<sup>4</sup>, R. Brakel<sup>2</sup>, B. Butterschoen<sup>2</sup>, T. Dittmar<sup>1</sup>, P. Drews<sup>1</sup>, F. Effenberg<sup>8</sup>, S. Elgeti<sup>4</sup>, O. Ford<sup>2</sup>, E. Fortuna-Zalesna<sup>9</sup>, G. Fuchert<sup>2</sup>, Y. Gao<sup>2</sup>, A. Goriaev<sup>10</sup>, A. Hakola<sup>11</sup>, T. Kremeyer<sup>2</sup>, M. Krychowiak<sup>2</sup>, Y. Liang<sup>1</sup>, Ch. Linsmeier<sup>1</sup>, R. Lunsford<sup>8</sup>, G. Motojima<sup>3</sup>, R. Neu<sup>4</sup>, O. Neubauer<sup>1</sup>, J. Oelmann<sup>1</sup>, P. Petersson<sup>12</sup>, M. Rasinski<sup>1</sup>, M. Rubel<sup>12</sup>, S. Sereda<sup>1,6</sup>, G. Sergienko<sup>1</sup>, T. Sunn Pedersen<sup>2</sup>, T. Vuoriheimo<sup>11</sup>, E. Wang<sup>1</sup>, T. Wauters<sup>10</sup>, V. Winters<sup>2</sup>, M. Zhao<sup>3</sup>, R. Yi<sup>1</sup> and the W7-X Team<sup>a</sup>
```

E-mail: s.brezinsek@fz-juelich.de

Received 14 June 2021, revised 23 September 2021 Accepted for publication 1 November 2021 Published 2 December 2021



#### **Abstract**

W7-X completed its plasma operation in hydrogen with island divertor and inertially cooled test divertor unit (TDU) made of graphite. A substantial set of plasma-facing components (PFCs), including in particular marker target elements, were extracted from the W7-X vessel and analysed post-mortem. The analysis provided key information about underlying plasma–surface interactions (PSI) processes, namely erosion, transport, and deposition as well

 $<sup>^{\</sup>rm a}$  See Klinger  $\it et~al~2019$  (https://doi.org/10.1088/1741-4326/ab03a7) for the W7-X Team.



<sup>&</sup>lt;sup>1</sup> Forschungszentrum Jülich, Institut für Energie- und Klimaforschung-Plasmaphysik, Partner of the Trilateral Euregio Cluster (TEC), 52425 Jülich, Germany

 $<sup>^2\,</sup>$  Max-Planck-Institut für Plasmaphysik, D-17491 Greifswald, Germany

National Institute for Fusion Science, National Institutes of Natural Sciences, Toki, Gifu 509-5292, Japan

<sup>&</sup>lt;sup>4</sup> Max-Planck-Institut f
ür Plasmaphysik, D-85748 Garching, Germany

<sup>&</sup>lt;sup>5</sup> JARA-HPC, Jülich Supercomputing Centre, Forschungszentrum Jülich GmbH, Jülich 52425, Germany

<sup>&</sup>lt;sup>6</sup> University of Wisconsin - Madison, Engineering Physics, Madison, WI 53706, United States of America

<sup>&</sup>lt;sup>7</sup> Southwestern Institute of Physics, PO Box 432, Chengdu, Sichuan, 610041, China

<sup>&</sup>lt;sup>8</sup> Princeton Plasma Physics Laboratory, Princeton, NJ 08540, United States of America

<sup>&</sup>lt;sup>9</sup> Warsaw University of Technology, 02-507 Warsaw, Poland

<sup>&</sup>lt;sup>10</sup> Laboratory for Plasma Physics, Ecole Royale Militiare/Koninkllijke Militaire School, B-1000 Brussels, Belgium

<sup>&</sup>lt;sup>11</sup> VTT, PO Box 1000, 02044 VTT, Finland

<sup>&</sup>lt;sup>12</sup> Royal Institute of Technology (KTH), Se-10044 Stockholm, Sweden

<sup>\*</sup> Author to whom any correspondence should be addressed.

as fuel retention in the graphite components. The net carbon (C) erosion and deposition distribution on the horizontal target (HT) and vertical target (VT) plates were quantified and related to the plasma time in standard divertor configuration with edge transform  $\iota = 5/5$ , the dominant magnetic configuration of the two operational phases (OP) with TDU. The operation resulted in integrated high net C erosion rate of 2.8 mg s<sup>-1</sup> in OP1.2B over 4809 plasma seconds. Boronisations reduced the net erosion on the HT by about a factor 5.4 with respect to OP1.2A owing to the suppression of oxygen (O). In the case of the VT, high peak net C erosion of 11  $\mu$ m at the strike line was measured during OP1.2B which converts to 2.5 nm s<sup>-1</sup> or 1.4 mg s<sup>-1</sup> when related to the exposed area of the target plate and the operational time in standard divertor configuration. PSI modelling with ERO2.0 and WallDYN-3D is applied in an interpretative manner and reproduces the net C erosion and deposition pattern at the target plates determined by different post-mortem analysis techniques. This includes also the <sup>13</sup>C tracer deposition from the last experiment of OP1.2B with local <sup>13</sup>CH<sub>4</sub> injection through a magnetic island in one half module. The experimental findings are used to predict the C erosion, transport, and deposition in the next campaigns aiming in long-pulse operation up to 1800 s and utilising the actively cooled carbon-fibre composite (CFC) divertor currently being installed. The CFC divertor has the same geometrical design as the TDU and extrapolation depends mainly on the applied plasma boundary. Extrapolation from campaign averaged information obtained in OP1.2B reveals a net erosion of 7.6 g per 1800 s for a typical W7-X attached divertor plasma in hydrogen.

Keywords: Wendelstein 7-X, graphite, erosion and deposition, plasma—surface interactions, material migration

(Some figures may appear in colour only in the online journal)

#### 1. Introduction

Wendelstein 7-X (W7-X) [1] is, next to the large helical device (LHD) [2], the currently largest operating stellarator in the world with a plasma volume  $V_P$  of 30 m<sup>3</sup> and a large radius R of 5.5 m. W7-X finished successfully its first operational phase in island divertor configuration using the so-called test divertor unit (TDU) [3]. Plasma-facing components (PFCs) made of fine grain graphite, designed to sustain power loads of 8 MW m<sup>-2</sup> without active cooling [4], were used to exhaust the plasma particle and power in the 3D-geometry of the toroidal device with five-fold symmetry [5]. Figure 1 shows schematically the horizontal target (HT) and vertical target (VT) plates of the 5 upper (u) and 5 lower (l) divertor half modules (HM) forming the TDU.

No significant damage occurred to the ten divertor modules in the executed 3.6h of integral operation in hydrogen (H) and helium (He) plasmas. The carbon (C) divertor with a total area of 25 m² received peak heat loads up to 10 MW m $^{-2}$  and thus 25% more than originally specified without harming the inertially cooled PFCs [4]. Up to 200MJ energy was coupled successfully into the electron cyclotron resonance (ECR) heated plasma discharges with a maximum duration of 100 s owing to its super-conducting magnetic field coils with B = 2.5 T on axis. The corresponding particle exposure with peak fluxes up to few  $10^{23}$  ions m $^{-2}$  s $^{-1}$  to the divertor and up to a few  $10^{21}$  ions m $^{-2}$  s $^{-1}$  to the first wall—consisting of graphite heat shields, graphite baffles, and stainless steel panels—resulted in a manifold of plasma—surface interactions (PSI) processes in

the complex geometry with island divertor. The W7-X operation with TDU was executed in two temporally separated operational phases (OPs), so-called OP1.2A (3776 s in mixed H + He plasmas) and OP1.2B (9054 s in H plasma), permitted in-between vessel access and exchange of dedicated PFCs. This included marker-coated target elements for PSI studies, marked in blue in figure 1, addressing material migration (erosion, transport, and deposition) and fuel retention presented in this contribution.

Main difference from perspective of PSI between OP1.2A and OP1.B is the application of boronisation in order to improve the wall conditions and provide access to operation at high core density around  $n_{\rm e}^{\rm c}=1\times10^{20}~{\rm m}^{-3}$  [6]. In view of upcoming steady-state operation, these PSI processes will determine the lifetime of divertor PFCs, the fuel cycle and plasma control, as well as the C dust production. The goal for the next operational phases in W7-X is the full exploitation of the super-conducting coil capabilities with new actively cooled PFCs made of carbon-fibre composites [7] in high density, long-pulse discharges up to 1800 s duration for which the TDU and the initial exploration of the island divertor in OP1.2A and OP1.2B laid the foundation.

Here, we focus on the analysis of these PSI processes carried out in the predominant magnetic configuration in both campaigns: the standard divertor configuration with edge transform  $\iota_a = 5/5$  discussed in more detail in section 2. This contribution includes studies at the main zones of interaction visualised *in situ* by infra-red (IR) thermography [8] as well as in-vessel by optical inspection of the HT and the VT plates

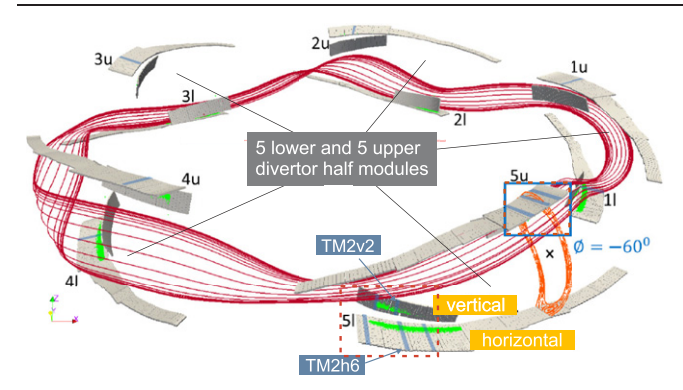


**Figure 1.** Island divertor arrangement in W7-X with its five-fold symmetry and five upper and five lower divertor HMs. Vertical and horizontal target plates equipped with a set of marker-coated target elements (blue). A bunch of field lines (red), their intersection with the target plates (green) in standard divertor configuration, and a 2D cut of the magnetic topology at the toroidal location of TM2h6 in HM 5u is shown as Poincare plot (orange). Reproduced courtesy of IAEA. Figure from [8]. © 2019 EURATOM.

[9]. In section 3, the impact of boronisation on the impurity influx into the confined plasma [10] as well as the oxygen (O) gettering in deposited boron (B) layers is discussed. Section 4 provides the erosion/deposition pattern on the VT and HT measured at representative marker target elements for both campaigns via ion beam [11] and laser ablation analysis [12]. This results in provision of net C erosion rates for typical attached divertor plasma conditions in standard divertor configuration with TDU. In section 5, PSI and impurity transport modelling with ERO2.0 [14] and WallDYN-3D [15] are applied to interpret the experimental findings on basis of a representative plasma background modelled with EMC3-EIRENE for W7-X [16, 17]. A brief summary and conclusions for OP2 are drawn in the last section 6.

#### 2. TDU and island divertor configuration

#### 2.1. Magnetic topology in standard divertor configuration

The so-called standard (magnetic) divertor configuration (EJM) with edge transform  $\iota_a=5/5$  and five magnetic islands cutting the target plates in the five modules of the stellarator is one of the best-diagnosed W7-X divertor configurations owing to a large set of dedicated edge diagnostics [18–21]. The shape of the TDU follows toroidally the form of the magnetic topology with intersection of the five magnetic islands by the target plates as depicted in figure 1 where the corresponding field lines hitting the target plates are marked as green dots [8]. The plasma shape varies thereby from the bean shape—marked in figure 1 by the Poincare plot at the toroidal angle  $\phi=-60^\circ$  of the torus—to the triangular shape multiple times in W7-X reflecting the five-fold symmetry of the device.

Figure 2(a) shows enlarged the intersection (2D cut) of two magnetic islands in standard divertor configuration with the VT and HT plates at one HM [22] close to the location of the marker target elements TM2v2 and TM2h6, which stands for target module 2 vertical 2 and horizontal 6, respectively. The cut of the islands by the target plates close to the X-point,

thus, close to the pumping gap (PG) between the VT and HT, marks the dominant interaction zone of the edge plasma with the PFCs. The projection of the cut in toroidal direction represents the main strike lines (dark red). Secondary strike lines (light red), poloidally further away from the PG on the VT and HT plates, exist, but show usually less pronounced PSI. The main interaction area is depicted in figure 2(b), where for the very same configuration the heat load footprint, measured during plasma exposure by IR thermography, is given. The actual extension of the interaction is determined by the impinging ions and electrons and depends on the magnetic configuration, the radiated power in the divertor, and—finally—the power load reaching the graphite target plates. Effectively, only a fraction of about 10% of the total VT and HT surfaces are used for heat exhaust in this configuration.

Detailed information about the actual interaction area, or more precisely, the power width equivalent to an integrated power decay length at the target plates in tokamaks, and its dependence on power arriving at the target and on the divertor state is given in [23]. Here, it is relevant that the area of impinging particles, or better, the impinging protons in hydrogen plasmas and impurity ions causing the heat flux deposition, can in first order be correlated to the area of gross erosion due to physical and chemical sputtering of graphite under ionizing divertor plasma conditions. The absolute magnitude of erosion depends on the flux distribution and the strength of chemical erosion in these plasmas. Interaction zones of other magnetic configurations like high mirror (KJM) or high iota (FTM) have to a large extent no significant overlap with the standard divertor configuration on the HT and, with some limitations regarding toroidal positions, on the VT plate, thus, the PSI processes in the divertor can in first approximation and under consideration of the corresponding operational time be separated between the different configurations (see overview in appendix A). However, the change from standard divertor configuration to e.g. high iota can potentially lead to deposition of previously erosion-dominated areas in standard divertor configuration, as these divertor areas are now shadowed, recessed from the plasma like first wall elements.

#### 2.2. PFC and marker target elements

The W7-X standard divertor configuration was the predominant magnetic configuration in OP1.2A (2481 s or 66% of time in H and He plasma mixtures) and in OP1.2B (4809 s or 53% of time in mainly H plasma). The operational time includes all types of divertor plasma conditions accessible in W7-X with TDU as well as moderate modifications of the interaction zones by application of corrections coils, reversed field operation, or plasma-induced currents in OP1.2B. However, those modifications were very limited in time; predominantly, plasmas with typically 10 s duration, attached divertor conditions, and medium ECR heating power ( $P_{\text{ECRH}}$ ) of about 3.0 to 4.0 MW were carried out. Therefore, in the first order approximation, the unmodified magnetic footprint in standard divertor configuration in attached divertor plasma conditions with medium ECR heating power can be identified as a campaignintegrated average and be related to results from post-mortem

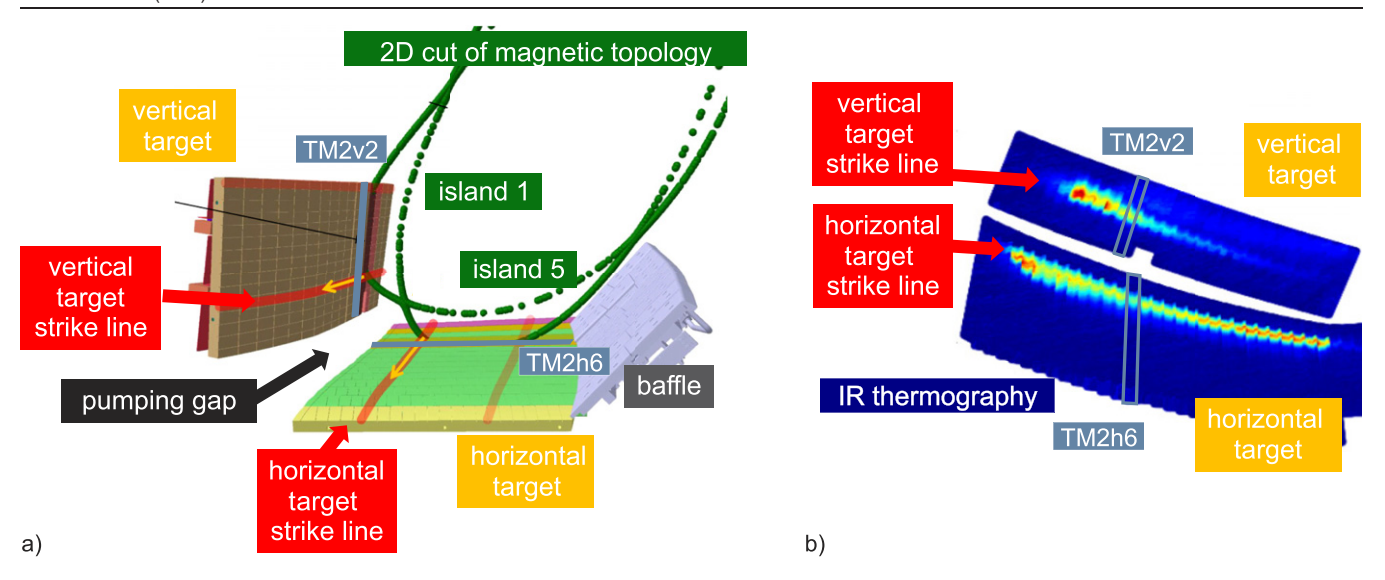


**Figure 2.** 2D poloidal cut of the magnetic topology in standard divertor configuration with two islands intersecting the target plates of one HM (cf). The strike lines on the HT and VT plates (red) as well as the position of two key marker target elements TM2v2 and TM2h6 (blue), and the PG are marked. Reproduced from [22]. ⊚ IOP Publishing Ltd. CC BY 3.0. (*b*) Corresponding IR thermography footprint on the HT and VT plates for the same configuration at the lower module 2 (cf [23]).

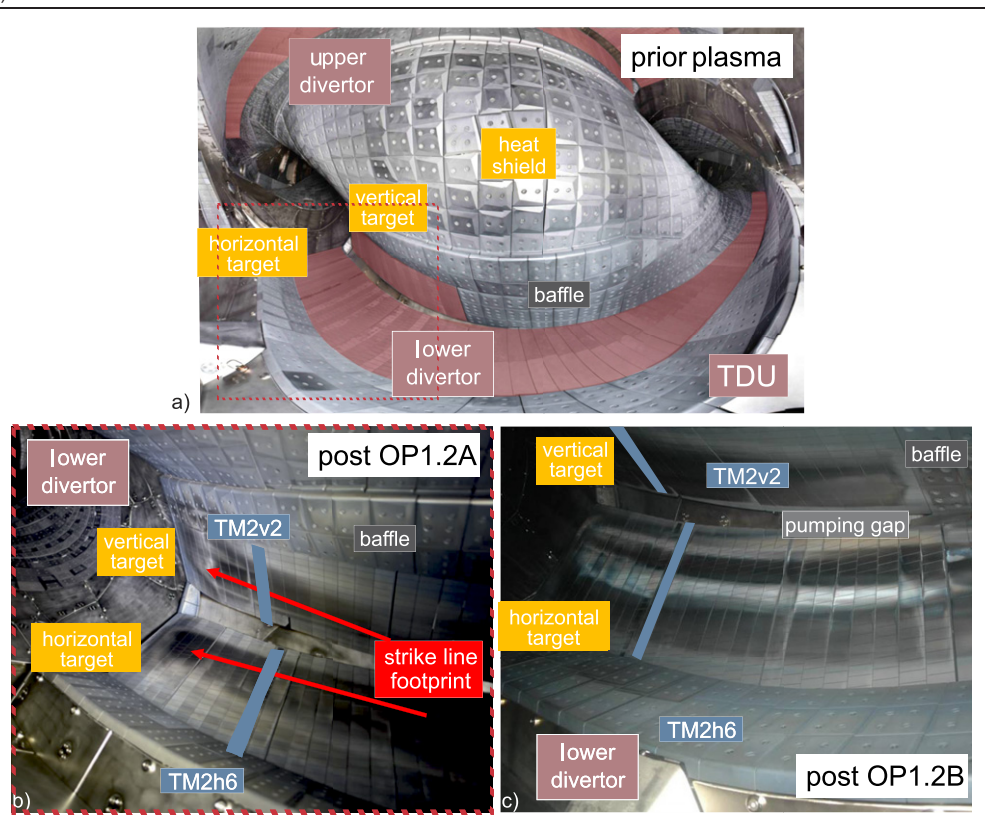
analysis of exposed PFCs obtained at the end of OP1.2A and of OP1.2B. Note that in general the post-mortem examined PFCs discussed in this contribution were installed in W7-X for only one campaign which permits the relation to plasma exposure in OP1.2A or OP1.2B. A high fidelity comparison between a single plasma background and post-mortem analysis describing C migration in a full-C device requires a tracer injection experiment in a single type of configuration and plasma at high fluence at the end of the operational campaign, thus, directly before the extraction of PFCs and further operation which can smear the PSI footprint. Such experiment with <sup>13</sup>CH<sub>4</sub> tracer was carried out in W7-X in OP1.2B and will be discussed in more detail section 5.3. It complements the campaign integrated analysis.

Figure 3(a) shows the interior of W7-X before the first plasma operation with TDU and pristine PFCs made of fine grain graphite (SGL 6710) for divertor ( $A_{\rm div} \simeq 25~{\rm m}^2$  in pink), heat shield ( $A_{\rm hs} \simeq 47~{\rm m}^2$ ), toroidal divertor closure ( $A_{\rm tdc} \simeq$ 3 m<sup>2</sup>), and baffle region ( $A_{\text{baf}} \simeq 33 \text{ m}^2$ ) [24]. Other first wall areas have largely stainless steel ( $A_{\rm fw} \simeq 77~{\rm m}^2$ ) on the plasmafacing side. The divertor target plates (VT and HT) consist itself out of a large set of so-called target fingers (typical dimension: HT 593 mm  $\times$  53 mm and VT 361 mm  $\times$  53 mm) and cover a total area of 19 m<sup>2</sup> capable to cope with high heat fluxes of 8 MW m<sup>-2</sup> during plasma operation. The first wall graphite components are designed to sustain a heat load between  $0.25 \text{ MW m}^{-2}$  and  $0.5 \text{ MW m}^{-2}$  depending on their location and purpose. All PFCs in OP1.2A and OP1.2B are inertially cooled to room temperature which is also the nominal temperature of the W7-X vessel. A photo of the vessel interior of one lower HM after OP1.2A plasma exposure is shown in figure 3(b) and can be compared with the pristine PFCs within the red rectangular box in figure 3(a). A change of the graphite surface morphology can be observed by the appearance of darkening stripes, which reproduce the strike zones on the VT and HT plates in standard divertor configuration.

Colorimetric analysis [25] performed in-vessel at the end of each operation phase provides non-destructive 2D information about the changes in reflectivity and optical properties of first wall surfaces. A photo of the W7-X vessel interior after OP1.2B, thus integrating for the majority of plasma-facing components the operational time in OP1.2A and B, is shown in figure 3(c). Figure 4 depicts the colorimetric analysis of (a)the HT plate and (b) the VT plate in HM 4u after OP1.2A (top) and after integrated plasma exposure in OP1.2A and OP1.2B (bottom). The RGB-values are averaged over the target finger substructures (graphite blocks) with a typical dimension of 25 mm × 55 mm. The RGB-values, which represent a measure of the reflected light composition in spectral dimension [26], are shown as function of the poloidal s and toroidal coordinate t. The PSI footprint on both target elements, complementary to the previously discussed IR footprint, are clearly visible for the measurements after OP1.2A though it cannot be concluded at this stage, if the changes in reflectivity and optical properties of the graphite divertor surfaces are caused by either erosion or thin deposition. The interpretation is more complex after OP1.2B where e.g. on the VT the variations in RGB-values are no longer distinguishable.

Complementary, marker target elements (figure 5), denoted as TM2v2 and TM2h6 in blue in figure 5(b) and made out of several individual graphite tiles, were utilized to measure, after extraction from the vessel, the campaign-integrated erosion and deposition pattern on the target plates in poloidal direction at dedicated toroidal positions in all HMs of the TDU. Both techniques together give a full insight in the erosion/deposition pattern in the vessel including potential asymmetries.

The marker target elements (figure 5(a)) consist of a C top layer with about 10  $\mu$ m thickness and a molybdenum



**Figure 3.** (*a*) View into the pristine W7-X vessel at one of the five modules showing a full lower HM and a part of an upper HM made of graphite PFCs prior to any plasma operation (cf [9]). (*b*) Photo of one lower divertor HM after plasma operation in OP1.2A. The darkened interaction areas on the VT and HT plates represent erosion zones and correspond to the strike-lines (red) in standard divertor configuration. (*c*) Photo of one lower divertor HM at end of TDU operation accumulating plasmas in OP1.2A and OP1.2B. The whitish zone on the HT is caused by an area of deposition with B content.

(Mo) interlayer with about 200 nm thickness deposited on the bulk graphite substrate of the target elements with the aid of the established combined magnetron sputtering and ion implantation technique (cf [11, 27]). The layers are precharacterized by elastic backscattering spectrometry (EBS by protons) before installation in W7-X. Post plasma operation, ex situ analysis allows the absolute quantification of erosion or deposition with respect to the Mo interlayer as demonstrated e.g. in [11] by EBS or in [12] by laser-induced breakdown spectroscopy (LIBS). Figure 5(b) shows three blocks of one castellated tile embedded in one marker target element after exposure in OP1.2A, where strong erosion took place and part of the layers vanished; the initial marker layer area is indicated by the blue rectangle. Figures 5(c) and (d) depict enlarged scanning electron microscope (SEM) images of focussed ion beam (FIB) cuts of a tile exposed in OP1.2B. The C top layer is in this example (figure 5(c)) largely intact and a local deposit of about 3  $\mu$ m could be identified. Close to the strike location, the C top layer is largely eroded and the Mo interlayer partially sputtered away at the top surface as shown in figure 5(d). Averaged net C erosion of more than 8  $\mu$ m occurred. Note the variation of the surface roughness on the SEM figures scale is indicating the initial high roughness of the graphite substrate and its porosity. Roughness is considered in data evaluation with EBS [13] and LIBS [28].

# 3. Impact of boronisations on PSI processes in W7-X

#### 3.1. Wall conditions in W7-X prior to boronisations

A wall conditioning cycle with initial vessel baking at  $150^{\circ}$ C for a week, followed by hydrogen glow discharge cleaning (GDC) for about 1h was applied after installation of the TDU and prior to the first divertor plasma operation in W7-X (OP1.2A) as described in detail in [29]. Though effective reduction of  $H_2O$ ,  $O_2$ , CO, and  $CO_2$  could be achieved before plasma ignition, the actual stellarator plasma operation was strongly affected by impurity radiation and hydrogen outgassing throughout the campaign. Regular inter-day GDC in H and He were done as well as effective inter-shot ECRH cleaning developed and applied to control the plasma density in particular in OP1.2A [29, 30].

Most critical from perspective of radiation-induced density limits in OP1.2A [6] is the presence of O and C in the plasma edge leading to an effective charge  $Z_{\rm eff}$  of up to 3.5 and causing a highly radiative edge mantle. A radiative collapse of the plasma occurred before high core density operation was achieved. The origin of O in the full-C device can be attributed to oxide layers at recessed areas of the first wall, to potential vacuum leaks, as well as to contamination of PFCs with water ( $H_2O$ ). The strongest contributor to the O content in OP1.2A

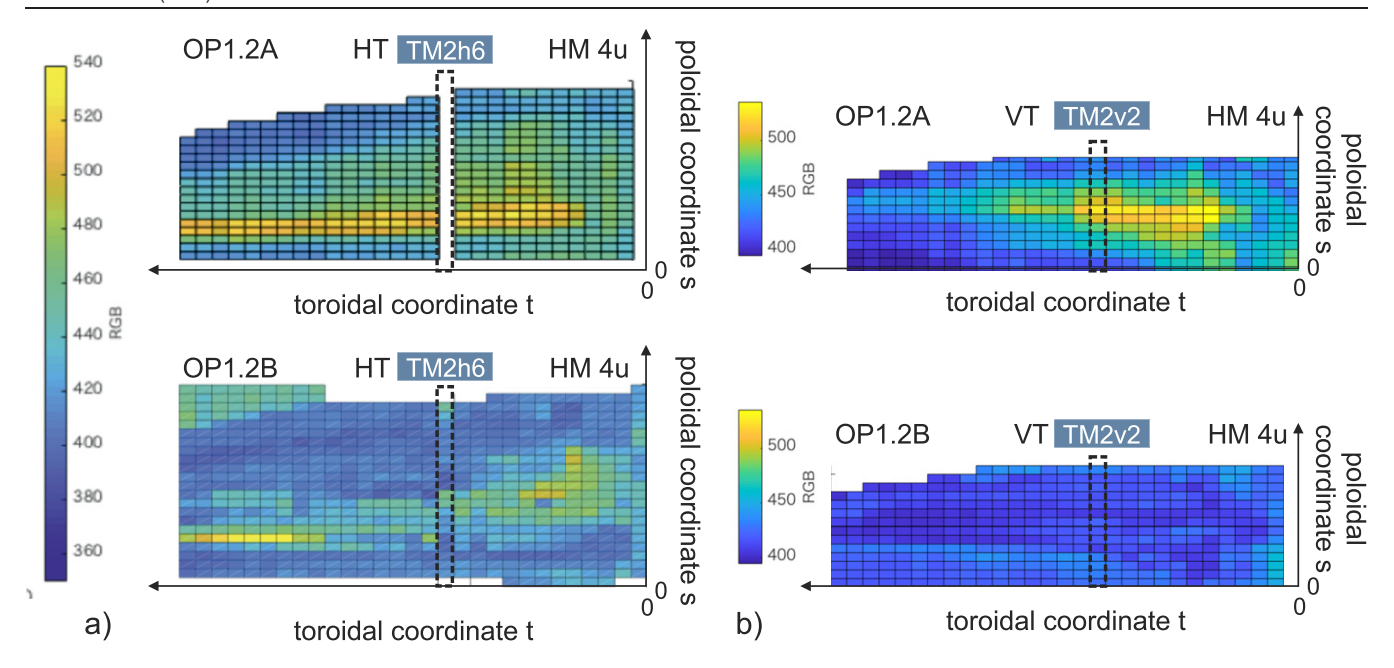


**Figure 4.** Colorimetric analysis of upper half module 4 (HM 4u) after OP1.2A and after integrated plasma exposure in OP1.2A and OP1.2B. Spatial distribution of the RGB-values over (a) the HT and (b) the VT plate of HM 4u.

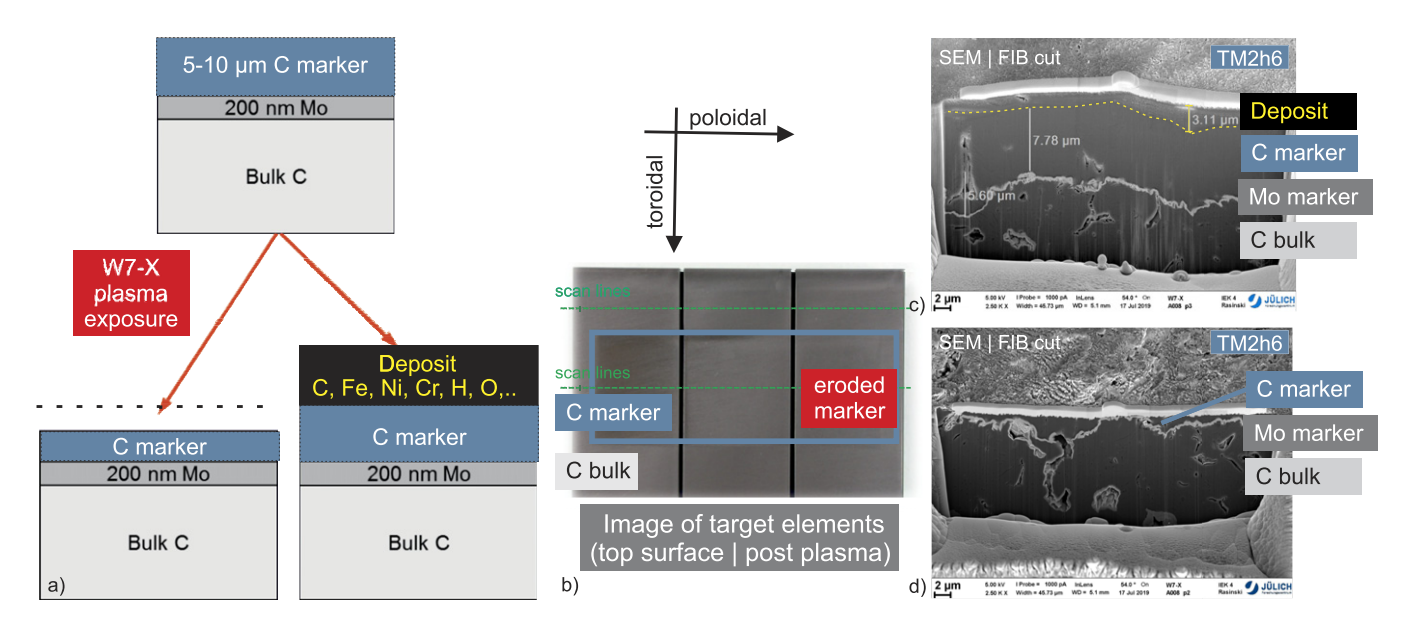


**Figure 5.** (*a*) Set-up and principle of C marker target elements with C top layer, Mo interlayer, and bulk graphite substrate as used for all marker elements including TM2h6 and TM2v2 fingers [11]. (*b*) Photo of an exposed target element tile with partially eroded top C marker layer (blue). The EBS and LIBS scanning lines for analysis are marked (green). (*c*) The different layers of the marker element are shown in a SEM/FIB cut including a deposited layer on top due to plasma operation in OP1.2B. (*d*) Corresponding SEM/FIB cut of a tile in the net erosion zone close to the strike line.

plasmas had been identified to be the water contamination of graphite divertor PFCs, though the target elements had been baked out prior to the installation to temperatures up to  $475^{\circ}$  C. This conclusion was drawn from intra-shot analysis of divertor spectroscopy on OI and OII representing the O source term [32], and intra-day analysis of O and O-containing molecules in the inter-shot residual gas spectrum of the W7-X vacuum [29]. A typical spectrum in the divertor covering  $H_{\gamma}$  and strong OII lines underlying the strong O source term in OP1.2A is given in figure 6(a).

The temperature of the inertially cooled divertor PFCs rises due to plasma loading during a day typically to 250°C until an equilibrium between plasma-induced bulk temperature rise and inter-shot cool down occurs. Water in the PFCs can be released and partially pumped out [29], but some residual O remains in the vessel [10]. The release is not homogenous from the PFC surface, but related to the heat load footprint as well as the achieved bulk temperature of tiles of a divertor finger. Consequently, the desorption process continues with rising input power and surface temperature or by change of the PSI zone by

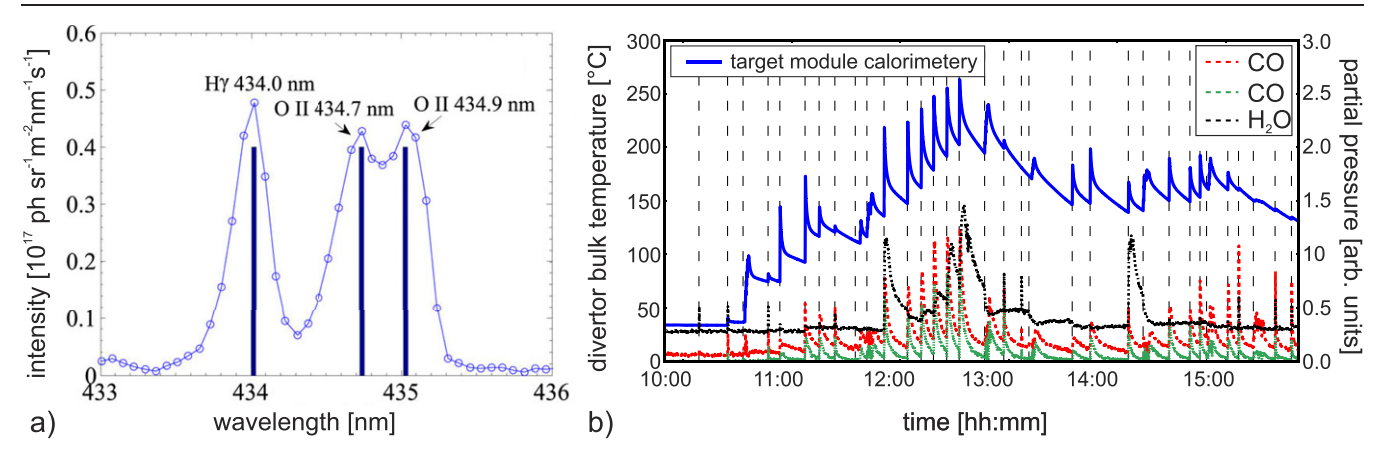


Figure 6. (a) Divertor emission spectrum showing  $H_{\gamma}$  and OII taken in OP1.2A [31]. (b) Temporal evolution of  $H_2O$ , CO,  $CO_2$  in the residual gas composition during the last day of operation prior to the first boronisation in OP1.2B. PFC bulk temperature evolution measured by calorimetry in HM 5u close to the strike-line location. The vertical bars indicate individual discharges of the experimental day. Reproduced courtesy of IAEA. Figure from [10]. © EURATOM 2020.

e.g. change of the magnetic configuration. Figure 6(b) shows the temporal evolution of the main O-containing molecules in the residual gas spectrum in W7-X at the last day before the boronisation. The increase of O-containing species with operational time and accompanied rising PFC temperature in the divertor is visible. The deposition of energy by plasma load and associated heating of the bulk graphite elements is effectively conditioning the PFCs up to the achieved PFC bulk temperature which explains the quiet start-up behaviour up to 150°C and the rise of O-containing molecular release in the next pulse. Intra-shot ECRH wall conditioning discharges were applied to reduce the O as described in [30]. But, not only O contributes to the plasma edge radiation, but also C, physically and chemically eroded by impinging O ions during plasma operation. Thus, the C sputtering is not solely determined by proton impact, but by impurity ion impact, namely O and C ions (self-sputtering), too. This behaviour was observed in other carbon wall devices before and cured by the application of boronisations [33].

#### 3.2. Impact of boronisation on impurity sources in W7-X

Access to the stellarator-favourable high density operational regime [6] was only possible owing to boronisations in OP1.2B, thus, glow discharges in a  $10\%B_2H_6 + 90\%He$  mixture, which deposits a thin B layer on the top surfaces of the first wall and divertor PFCs and getters O. Moreover, the surface coverage also prevents further transient release of water from the graphite plasma-facing sides. Figure 7(a) shows CII and OII emission spectra of singly ionised C and O in the divertor before and directly after the first application of a boronisation in W7-X. The emission spectra of these singly ionised C and O—representing the divertor impurity source—were recorded in a pair of hydrogen discharges with identical plasma input parameters and magnetic configuration. The line emission is normalised to the  $H_{\gamma}$  emission reflecting the recycling flux and reveals a dramatic local reduction of the O and the C source close to the strike line where the line-of-sight of the spectrometer was positioned. The impurity content in the plasma core, measured with the VUV HEXOS [35] system behaves accordingly as depicted in figure 7(b). The reduction of impurities is in-line with the reduction of the effective plasmas charge  $Z_{\rm eff}$ , a measure for the plasma purity, which drops from typically 3.5 in OP1.2A to 1.5 in OP1.2B. Figure 7(c)shows the temporal evolution of the normalised B (BII at 703.1 nm), C (CII at 426.7 nm), and O (OI at 844.5 nm) edge emission, over the campaign OP1.2B for comparable discharges and magnetic configurations indicating a reduction of O by more than a factor 10 and the C by a factor 7 with respect to the pre-boronisation values [10]. Moreover, figures 7(c) and (d) reveal the rise of the normalised C divertor influx and O core content after a boronisation, which can be attributed to the re-erosion of the B layer at the location of the spectroscopic measurement and exposure of the graphite divertor to the plasma. The O influx rises slower, which suggests, that a fraction of the O is permanently bound or pumped away by the B; the O source attributed to the divertor is on a longer time scale significantly reduced.

Figures 8(a) and (b) are showing evidently the capture of O by B layers from boronisation and the associated reduction of C in the post-mortem analysis (SEM, FIB and energy dispersive x-ray analysis (EDX)) of a sample taken from the divertor target element TM2h6 which were located in a netdeposition zone with maximum observed thickness of 8  $\mu$ m. Three regular boronisations marked as B<sub>2</sub>H<sub>6</sub> were executed over the duration of the campaign OP1.2B. Three well separated broad B peaks in atomic weight, in-line with O peaks indicating the gettering process, are visible in depth of the FIB cut sample. Correlated are three dips in the C weight fraction confirming the layer-like structure visible in figure 8(b). Iron (Fe) is caused by first wall erosion during He GDC prior to the first boronisation which is also linked to O release due to erosion of surface oxides. Note that directly prior to the third boronisation, an in situ B deposition via B<sub>4</sub>C was performed by a powder injector system located at the midplane manipulator during plasma operation [36, 37]. About 1.5 g B was introduced into W7-X and deposited primarily on the target plates; this B is embedded the third broad B layer in figure 7(c). The origin of the additional B peak in the deposited

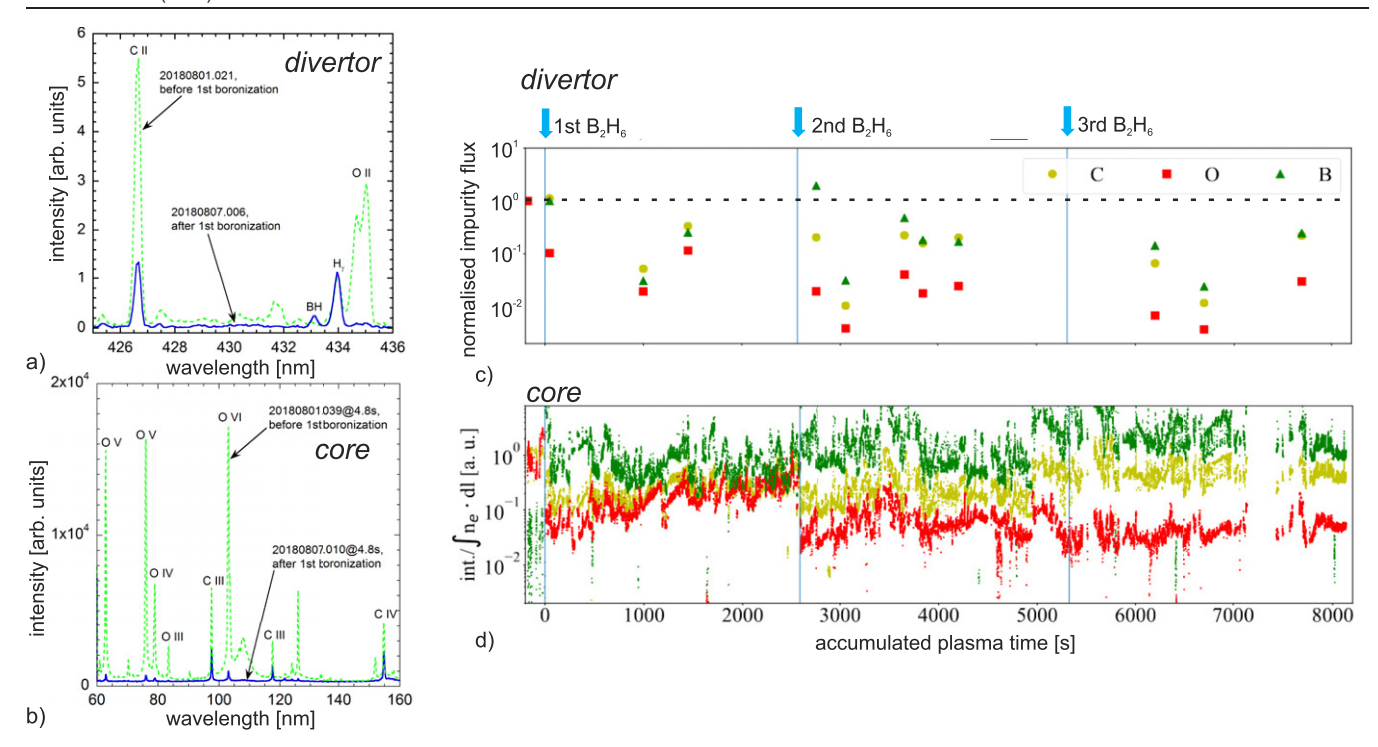


**Figure 7.** Impact of a boronisation on the impurity content in (a) the divertor and (b) core plasma of W7-X visualized by optical emission spectroscopy of C and O ions [34]. (c) Evolution of C, B, and O divertor source strength with accumulated plasma time in OP1.2B deduced from divertor spectroscopy of singly ionized C, B, and neutral O atoms (cf). (d) Long-term evolution of C, B, O core content over the plasma time in OP1.2B. Reproduced courtesy of IAEA. Figure from [10]. © EURATOM 2020.

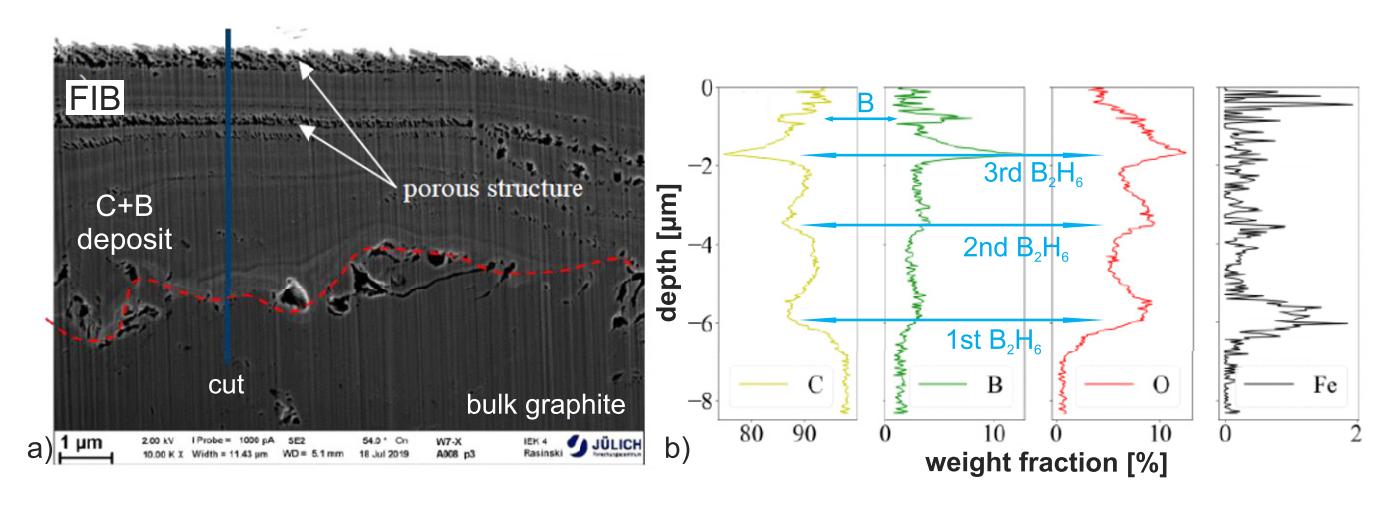


**Figure 8.** (a) FIB cut of target element TM2h6 in HM 5l with associated EDX line scan (blue) revealing local C, B, O, and Fe deposition on bulk graphite. (b) Three B and O peaks, anti-correlated with C dips, reflect the three boronisations in OP1.2B. Reproduced courtesy of IAEA. Figure from [10]. © EURATOM 2020.

zone about 1  $\mu$ m depth and 150 nm width is unknown and might be correlated to a change of magnetic configuration and B erosion from a previously untouched plasma-facing surface. The three boronisation introduced commutatively  $\simeq 18$  g into the vessel with 22% of B introduced in the first, 43% of B in the second, and 35% of B in the last boronisation in form of 10% B<sub>2</sub>H<sub>6</sub> diluted in the He glow discharge. These were the first boronisation in W7-X and some moderate optimisation in view of homogeneity and reliability took place with increasing number of boronisations, thus, the B deposition rate

and the B distribution in the vessel might be slightly different in the three boronisations. Assuming an equal distribution of boron on the W7-X vessel walls, the average B layer would have about 20-25 nm thickness per boronisation. Contrary, the appearance of B is much broader in the EDX analysis figure 8(a) indicating that the B deposition stems from multiple erosion/deposition processes and strong net-deposition at the analysed location. The executed plasma time in W7-X after a boronisation was comparable as indicated by the vertical lines in figure 7(d).

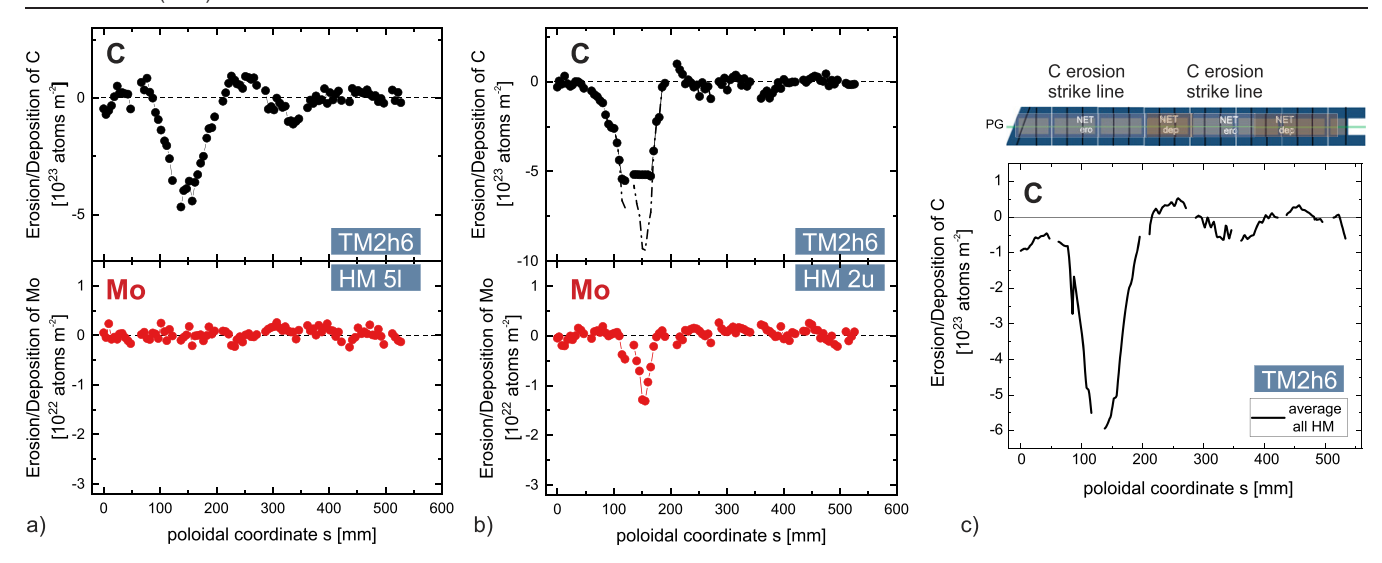


**Figure 9.** The C erosion/deposition pattern along the poloidal coordinate *s* of one horizontal target element TM2h6 from (*a*) the lower half module 5 and (*b*) the upper half module 2 deduced from differential EBS measurements before and after OP1.2B. (*c*) The averaged poloidal erosion/deposition profiles of all ten half modules of the test divertor unit.

The positive impact of boronisations on the wall conditions in W7-X can be separated (i) in a short-term effect related to the strike-line location and limited due to fast re-erosion of the B layer under high ion flux impact, and (ii) a long-lasting effect related to the first wall and limited by re-erosion due to the low impinging ion and charge-exchange flux. It can be seen that the long-lasting effect will be at least compatible with the duration of one long-pulse discharge of 1800 s in future. The boron dropper techniques can be applied to renew the B layer transiently on the divertor target plates as the deposition is related to the applied magnetic configuration and associated plasma fluxes of the plasma.

# 4. Erosion and deposition pattern in standard divertor configuration

#### 4.1. C erosion at the horizontal target plates

Two complete sets of C/Mo/C marker target elements, introduced in detail in section 2, were utilised to determine the net erosion of C integrated over the campaign OP1.2A and OP1.2B, respectively. In the case of OP1.2A and the high impurity content of O and C present in the plasma, the method was challenged as not only the C top layer was completely eroded at the strike-line location, but also large fractions of the Mo interlayer. The impact energy threshold for Mo erosion by mono-energetic protons is about 200 eV [38] and above the impact energies of impinging protons and chargeexchange hydrogen atoms in the normal operational window of W7-X. Thus, the main part of Mo erosion must be caused by impinging O and C ions which have a sputtering threshold energies of about 25-35 eV. Moreover, likely ionisation stages 3+ and 4+ dominate the impurity outflux in attached conditions, thus, in all divertor plasma conditions in OP1.2A, Mo has been sputtered if exposed to the surface. The peak C erosion locations in both campaigns is the same, whereas the

overall C erosion/deposition balance point varies due to reduction of the net C erosion source in OP1.2B owing to lower O and C content.

Figures 9(a) and (b) show examples of the net erosion/deposition poloidal profile on the HT plate at the location of TM2h6 in the lower half module 5 (HM 51) and the upper half module 2 (HM 2u) after plasma loading in OP1.2B [39]. The poloidal profile is given in format of the s coordinate with its origin at the pumping gap of the horizontal target. In both cases, the peak erosion is located at about s = 150 mm at the location of the inner strike line in standard divertor configuration as defined in section 2. A second, much weaker erosion zone is detectable around s = 350 mm away from the PG in poloidal direction. It coincides with the secondary strike line of the standard divertor configuration on the HT plate, though it also overlaps with the main strike line of the socalled low  $\iota$  configuration (DBM), which was used about 13% of the experimental time in OP1.2B in contrast to the dominant 53% in standard divertor configuration (see appendix A). Moreover, there are clear net deposition zones next to the main strike line close to the PG and between the two net erosion zones visible.

Though the C net erosion/deposition pattern of the two equally positioned TM2h6 marker target elements with respect to the HT geometry is qualitatively in very good agreement, they show a quantitative difference related to the stellarator module or to the up/down location. In the HM 2u case, not only the C top layer, but also the Mo interlayer was partially eroded and the peak net C erosion had to be extrapolated from the Mo erosion and consideration of the different sputtering yields as described in [11]. There is almost a factor 2 difference in the peak net C erosion between these two toroidal positions. In figure 9(c) is for comparison the averaged net C erosion/depositon profile of all ten half modules exposed in OP1.2B depicted. The discontinuity of the profile reflects

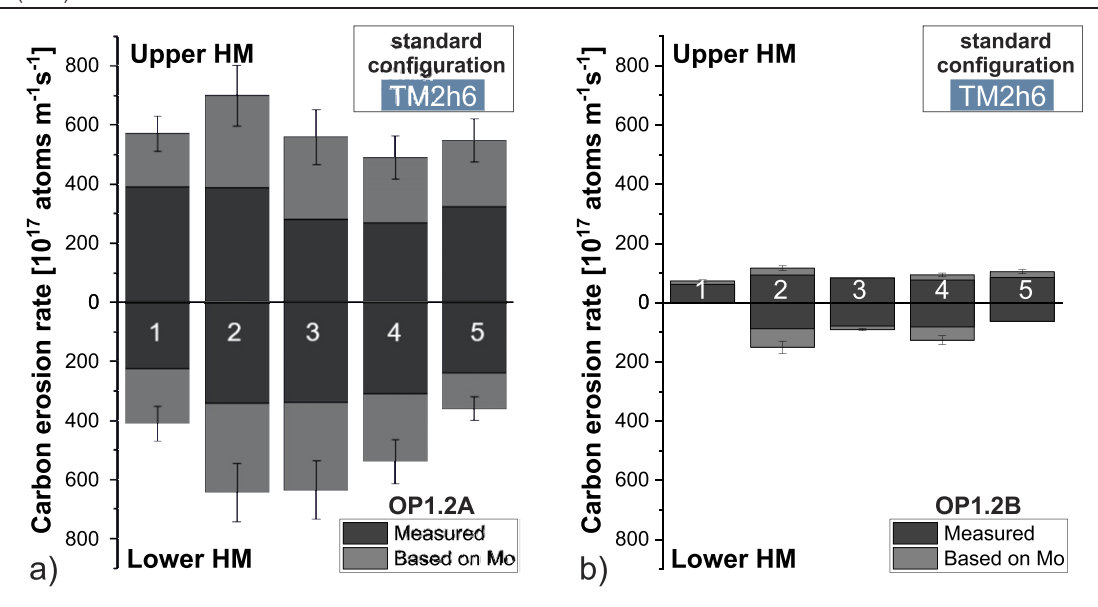


Figure 10. (a) Toroidal distribution of net C erosion rates of TM2h6 elements over all upper and lower half modules. The poloidally integrated net C erosion is normalised to the plasma time in standard divertor configuration in OP1.2A. (b) Corresponding net C erosion rates for OP1.2B executed with reduced impurity content due to boronisations. Reproduced from [11]. © 2020 The Royal Swedish Academy of Sciences. All rights reserved.

the gaps in the marker layer of TM2h6 which consist of 8 individual graphite tiles.

Figure 10 shows the variation of the poloidally integrated net C erosion rate of the complete element TM2h6 over the graphite HMs exposed. In a full symmetric arrangement, all 5 upper and 5 lower half modules shall have the same C erosion rate as they shall receive the same particle load. Variations in the heat load to the HMs have been observed before and related partially to imperfect positioning of HMs, which might also explain the variations in the impinging particle flux and net erosion as discussed in [11]. Moreover, an up—down asymmetry in the particle and heat fluxes due to particle drifts [40] has been recently identified; it might also contribute to the asymmetry in the erosion/deposition pattern of upper and lower half modules.

Figure 10(a) provides the net C erosion rate distribution over the HMs for OP1.2A where in all cases the extrapolation was done with the aid of the Mo interlayer erosion. Figure 10(b) gives the corresponding distribution for OP1.2B. The campaign-averaged net C erosion rate on the HT plate drops by a factor 5.4 between the first and second campaign with TDU in standard divertor configuration. The difference is attributed to the reduction of the impurity content due to application of boronisations in OP1.2B, where the C erosion is finally determined by proton-induced physical and chemical sputtering as well as C self-sputtering. The total net erosion of C per campaign at the horizontal target plates of the TDU can be extrapolated from the given EBS data from all marker target modules and under consideration of temperature footprint on the HT plate for the standard divertor configuration. The net C erosion amounts (34.5 + / - 8.4) g C in OP1.2A [11] and (13.7 + / - 2.3) g C in OP1.2B [39] or normalised to the exposure time solely in standard divertor configuration to a C erosion rate of (13.9 + / - 3.4) mg s<sup>-1</sup> in the mixed He + H

plasmas of OP1.2A (2481 s) and (2.8 + /0.5) mg s<sup>-1</sup> in the H plasmas of OP1.2B (4809 s).

#### 4.2. H retention at the horizontal target plates

Next to the EBS measurements, also LIBS and laser-induced ablation quadrupole mass spectrometry (LIA-QMS) measurements were carried out on the same horizontal target elements with marker layers (TM2h6) exposed in W7-X [28, 41]. Ion beam and laser-based methods agree well in the depth-resolved information of C and Mo and provide the erosion/deposition pattern in poloidal direction of the target plates at different toroidal locations. Additionally, LIBS and LIA-QMS have access to the H content and complement ion beam analysis techniques with respect to the hydrogen spatial and depth distribution as latter have no direct access to  $^{1}$  H.

Figure 11 gives an example of the laser-based analysis of marker target element TM2h6 installed in half module 1u and exposed to H + He plasmas in OP1.2A. Figure 11(a) depicts the complete target element with the eight individual tiles forming the target finger. The darkened area represents the net erosion zone at the main inner strike line which correlates with the peak-heat load zone in standard divertor configuration. An IR footprint for a representative discharge in standard divertor configuration in OP1.2A is shown for comparison. Figure 11(b) visualises the appearance and disappearance of the MoI line emission in the LIBS spectrum as function of the poloidal coordinate s on the marker target element TM2h6 in half module 1u (HM 1u). At each spatial location 200 laser pulses were executed in a row to obtain depth-resolved information and to determine erosion and deposition areas of the target element. The Mo interlayer acts as scale for depth resolution. The original marker structure (C/Mo/C) is still intact at the location s = 450 mm far from the strike lines. There

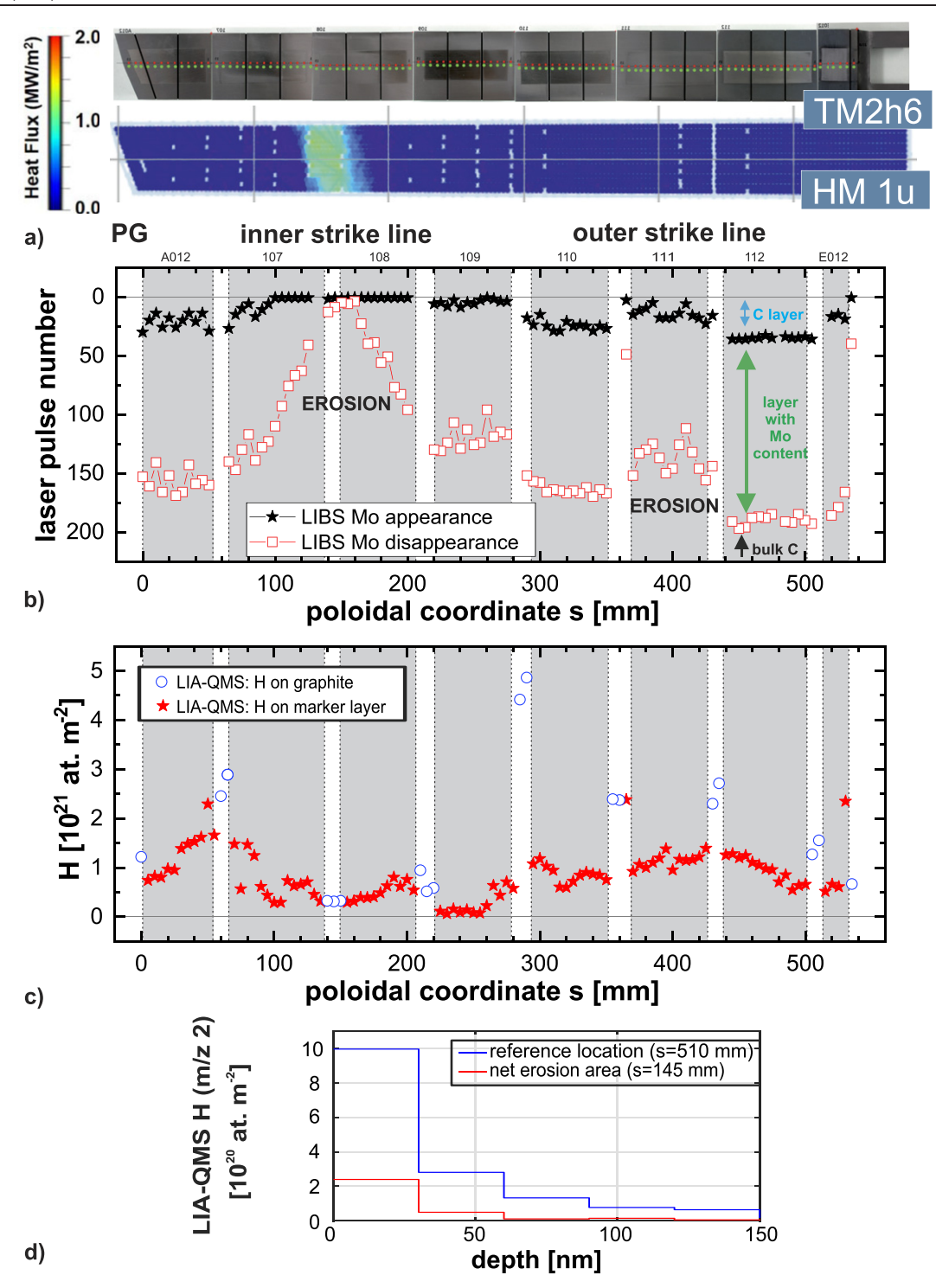


**Figure 11.** (*a*) Image of individual graphite tiles of target element TM2h6 in half module 1u extracted after OP1.2A and a typical heat load pattern for a representative discharge in standard divertor configuration. (*b*) Depth-resolved distribution of C and Mo at TM2h6 in poloidal direction measured by LIBS. (*c*) Complementary poloidal distribution of the campaign-integrated H content determined by LIA-QMS. (*d*) Depth-resolved H distribution at two representative locations: strong net erosion zone and at a virtual erosion-free zone.

is nor erosion neither deposition at this location without significant plasma particle loading and three different layers can be distinguished: the C top layer, a thick layer with detectable Mo content combined with C, and the pure graphite substrate. Full quantification of the erosion depth requires the characteristic ablation rates for the different materials present in the

marker layer, the laser characteristics, and material roughness as studied extensively in [28, 42] for PFC materials used in W7-X. The immediate appearance of MoI emission at the target element surface between s=80 and s=280 reflects the complete erosion of the C top layer in this part of the HT. Mo is eroded by O and C ions within this poloidal extension as

discussed before; the peak net erosion can be identified at the location s=150 mm where MoI emission fades away in the first LIBS pulse. This result confirms the spatial extension of the net erosion zone on the horizontal target element identified in EBS measurements [11] and shown in figure 10(a) for half module 1u. The comparison of figures 11(a) and (b) shows the good agreement of the peak net erosion and the peak heat load zones at the inner strike-line position of the standard divertor configuration in OP1.2A.

The main mechanisms for H retention in graphite are implantation and co-deposition [43]: co-deposition dominates in long-term operation as it is proportional to impinging proton flux and rises linearly with plasma operation time. Implantation in graphite is limited and takes place in the near surface followed by diffusion into the bulk material and depends on the material structure and temperature. In standard divertor configuration during OP1.2A are the HT and VT plates not in deposition zone, thus, co-deposition of H with C is negligible as retention mechanism in this case and solely implantation determines the fuel content in graphite. LIA-QMS [41] was applied to determine the spatial distribution of the H content in the surface of target element TM2h6 in half module 1u as depicted in figure 11(c). The total H content was accumulated in the first five consecutive laser pulses at the same location. Figure 11(d) shows the associated H depth profiles for two characteristic locations on the target element confirming the dominant appearance of H in the near surface of the target element and that five laser pulses are sufficient for the quantification. The original C/Mo marker layer on the graphite substrate is in poloidal direction not continuously deposited on the TM2h6 finger (figure 5(b)), but small spatial gaps with the fine grain graphite substrate at the surface exist between sets of individual tiles (see figure 5). These fine grain surfaces of TM2h6 are marked by circles in figure 11(c)) whereas the areas with (initial) C/Mo marker surfaces are labelled by stars. The measured integral H retention does in general not exceed  $1.6 \times 10^{21} \, \mathrm{Hm}^{-2}$  at areas with (initial) C/Mo marker layer. The H retention is as low as  $0.5 \times 10^{21} \, \text{Hm}^{-2}$  at the highest net C erosion at the strike-line location around s = 140-160 mm, where the surface temperature during plasma impact was highest and retention by implantation is correspondingly lowest. This is independent of the initial surface composition of the TM2h6 finger. Contrary, high H retention up to  $5 \times 10^{21} \, \mathrm{Hm}^{-2}$ has been measured on surfaces with fine grain graphite finish away from the strike area (e.g. at s = 280 mm) whereas the H retention was locally about a factor 5 higher at nearby areas with marker layer at the top surface (e.g. at s = 300 mm). The fine grain graphite applied as bulk material of the TDU has a higher porosity then the C top layer of the C/Mo marker surfaces as depicted in the cross-section in figure 5(c). The difference in porosity can explain the large difference in H retention within a few mm in lateral direction at otherwise similar surface temperature and impinging proton flux conditions during plasma operation. It must be stressed, that the total H content of the TDU is best represented by the measurements at the fine grain graphite surfaces (blue circles in figure 11(c)) indicating a high hydrogen reservoir between the inner and outer strike-line locations. This hydrogen reservoir contributes to the strong hydrogen outgassing observed in OP1.2A when the plasma touches these areas; areas that have not experienced high temperature excursions during plasma operation. The estimation of an overall retention rate is more than challenging as in OP1.2A mixed plasma operation in H and He took place and significant H was initially stored in the PFCs.

The situation changed in OP1.2B where also parts of the HT and VT plates were in deposition zone covered partially by boron layers as shown e.g. in 9(c). Thus, co-deposition at the target plates is in OP1.2B relevant as mechanism for hydrogen retention in PFCs of the TDU and must be taken in account in overall retention calculations. Further analysis of target elements exposed in OP1.2B are required to obtain an integral view of the H content. Note, co-deposition has been also identified during OP1.2A and OP1.2B at the baffle regions exposed at low surface temperature where carbon-containing layers of several  $\mu$ m thickness have been found. Peak retention up to  $1 \times 10^{22} \, \mathrm{Hm}^{-2}$  was measured in those co-deposits with up to 1.5  $\mu$ m C layer thickness after OP1.2A [41].

#### 4.3. C erosion at the VT plates

A similar comprehensive post-mortem analysis employing EBS and LIBS was carried out for the marker target elements TM2v2 embedded in the VT plates of the ten half modules of W7-X. An open point so far is the direct demonstration, that the heat load footprint derived from IR thermography correlates spatially with the impinging particle footprint which itself is responsible for the gross C erosion at the target pates. The latter, measurable by optical emission spectroscopy on low ionising C [44], feeds into the net C erosion footprint recorded at the target plate by post-mortem analysis, but the correlation is not direct as C deposition causes the difference between net and gross C erosion as well as can impact the IR thermography interpretation. The most suitable test case to establish a link between the heat flux (by IR) and the net C erosion distribution (post mortem analysis) is the comparison of both quantities in the case of a pure net C erosion zone under ionising conditions—like observed on the VT plate in OP1.2A.

Figure 12 depicts the net C erosion/deposition profile as function of the poloidal coordinate s at the toroidal location of TM2v2 in (a) the lower half module 5 (HM 5l) and (b) the upper half module 5 (HM 5u) derived from LIBS. As the measurements were executed after OP1.2A, strong impurity-induced sputtering occurred during plasma operation and total erosion of the C top layer and almost complete erosion of the Mo interlayer occurred. The peak net C erosion at 5l around s = 165 had to be extrapolated (green points) from the Mo interlayer erosion and amounts about 16.6  $\mu$ m or  $1.5 \times 10^{24}$  atoms m<sup>-2</sup> as shown in figure 12(a) [28]. This converts into a peak C net erosion rate of 6.7 nm s<sup>-1</sup> at this location when related to the plasma time in standard divertor configuration in OP1.2A (2481 s). Overlaid in the same figure is the poloidal heat flux profile at the toroidal location of TM2v2

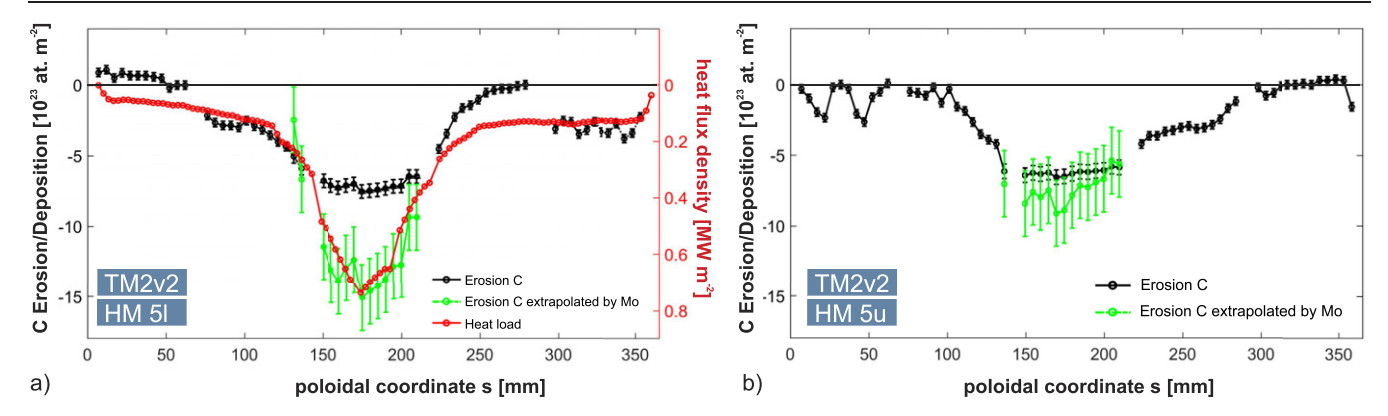


**Figure 12.** (a) Net C erosion and deposition profile of marker element TM2v2 exposed at HM 51 in OP1.2A . The heat flux footprint of a representative discharge in standard divertor configuration taken at the location of TM2v2 by IR thermography. Reproduced courtesy of IAEA. Figure from [28]. Copyright (2021) IAEA. (b) Net C erosion and deposition profile of marker element TM2v2 exposed at HM 5u in OP1.2A.

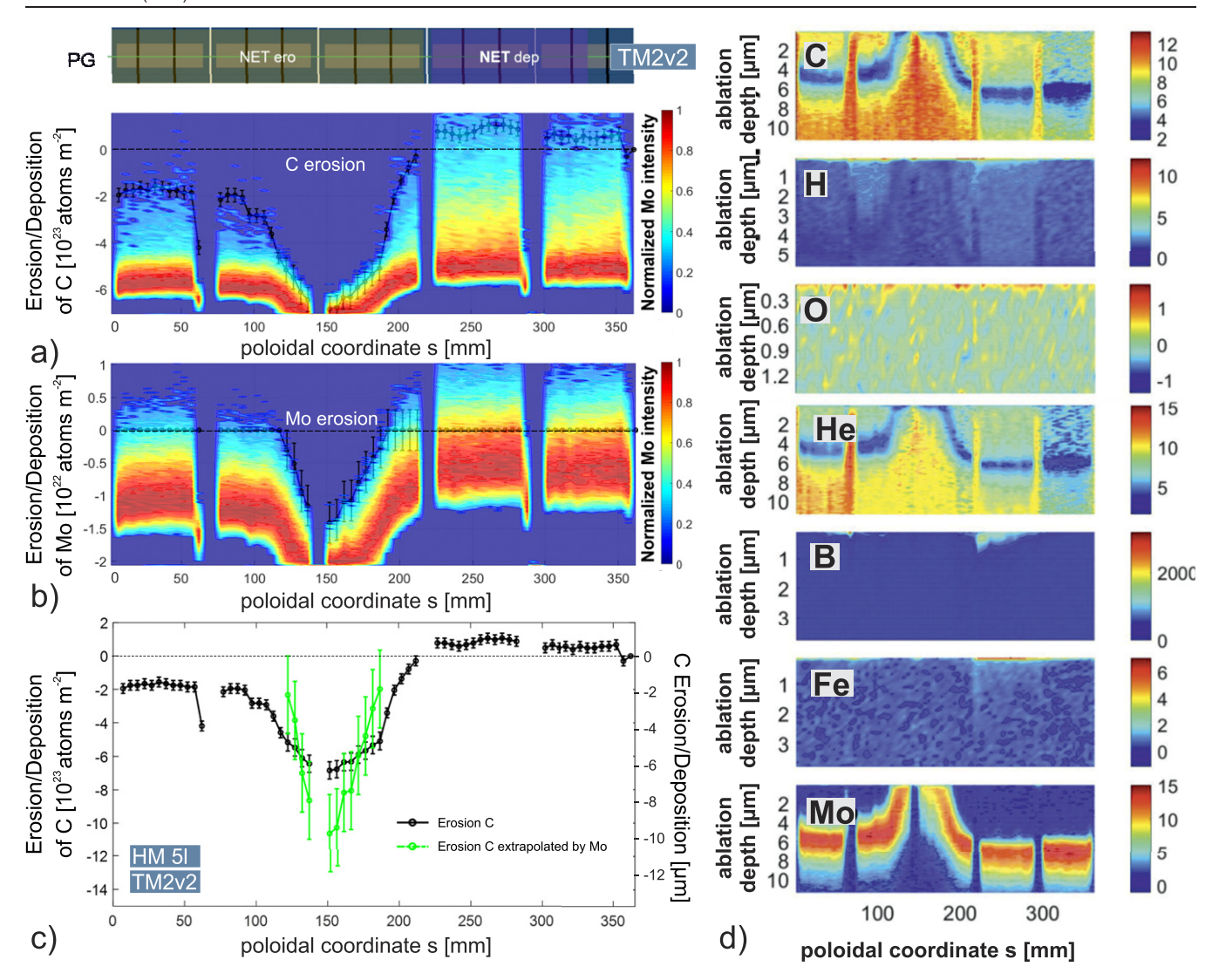
deduced from a representative discharge by IR thermography. The peak heat flux reflects the main magnetic strike line in standard divertor configuration on the VT. Both profiles show a good qualitative agreement in poloidal direction though they reflect different physical quantities: the impinging heat flux, the impinging particle flux, and the net C erosion distribution which stems from the competition of gross C erosion and C deposition. The PSI and impurity transport code ERO2.0 will be used in the next section 5.2 to connect these physics quantities for a better interpretation of the experimental data and their correlation.

Figure 12(b) describes the net C erosion and deposition profile along the poloidal coordinate s for the TM2v2 finger located in the upper half module 5. The main feature of the erosion and deposition profile, the wide net C erosion zone around s=165, preserves at the upper half module 5u in comparison with the previously discussed lower half module 5. However, the absolute magnitude differs substantially between the two HMs in the same module 5 of W7-X in OP1.2A. There is in particular only moderate Mo interlayer erosion; the extrapolated net C erosion in HM 5u amounts 10.1  $\mu$ m, thus, about 40% less than in HM 51. The discrepancy in net C erosion is comparable to variations observed at the HT plates. It is most likely related to top/down asymmetries in heat and particle loads due to plasma flows [40].

The corresponding LIBS analysis of TM2v2 in HM 5u reveals also strong net C erosion on the VT of the TDU after plasma operation in OP1.2B. Figure 13(a) shows complete erosion, 7.7  $\mu$ m at this toroidal location, of the C top layer around the strike line in standard divertor configuration (s=150 mm). Moreover, the Mo interlayer is strongly eroded by plasma particle impact as depicted in figure 13(b) and an equivalent of about 2.5  $\mu$ m of the mixed C/Mo layer is physically sputtered away. Please note, that the actual width of the Mo emission is not reflecting solely the thin Mo interlayer, but the material thickness where Mo and C co-exist in LIBS spectra. This is caused by the large laser spot size of 1 mm diameter and material roughness in the  $\mu$ m-range as discussed and modelled in [28] and depicted in figure 5(d). The peak net C erosion

needs to be reconstructed as before from the C top layer erosion and the partial Mo interlayer erosion (figure 13(c)) and amounts  $11.8~\mu m$  or  $1.06\times 10^{24}$  atoms m $^{-2}$  for TM2v2 at HM 51. This transfers into a peak net C erosion rate of 2.5 nm s $^{-1}$  when normalised to the operational time in standard divertor configuration in OP1.2B (4809 s). The peak value of the net C erosion rate at the same half module 51 drops only by a factor 2.7 from OP1.2A to OP1.2B. This reduction is only half the value observed on the HT plate at TM2h6. Additional net C erosion causes, e.g. due to operation in the high mirror configuration (KJM), need to be included in the analysis of the VT plates.

The application of boronisations in OP1.2B converted a part of TM2v2, and thus the VT plate, into a net deposition zone at s > 200 mm in the dominantly applied standard divertor configuration. The deposition is determined by a material mixture of C, B, O, Fe and H as characterised by the LIBS depth profiles in figure 13(d) derived from corresponding neutral or single ionised line emission of the deposited species [45]. The common deposition of B and O is related to the gettering of O by B as visualised in figure 9(b) taken in a deposition zone. The detected H in the near surface at poloidal locations with s > 200 mm is mainly caused by co-deposition with the low-Z impurities present in the deposition layer: B and C. Contrary, detected H at the surface in the moderate erosion zone at s < 100 mm is caused by implantation. Fe appears at the same poloidal locations as Be and O, but extends deeper in the surface. Fe is deposited primarily by He-GDC executed prior to the initial boronisation in OP1.2B. Subsequently, He GDCs were in OP1.2B omitted to a large extent, so that additional Fe sputtering from the steel panels was suppressed and associated deposition on the TDU prevented. Complementary LIBS analysis a few cm away from the marker area in toroidal direction on fine grain graphite part showed a similar deposition and depth pattern regarding the intrinsic impurities B, O, Fe including some Mo deposition. Mo originated from the Mo interlayer sputtering at the strike-line location and migrated with operational time in OP1.2B towards the nearby fine grain graphite surface.



**Figure 13.** Poloidally resolved erosion and deposition pattern of TM2v2 located in HM 51 after exposure in OP1.2B: (*a*) marker C layer erosion, (*b*) Mo interlayer erosion, and (*c*) extrapolated total net C erosion. (*d*) Complementary depth-resolved composition analysis of C, H, O, He, B, Fe, Mo at the target elements surface by LIBS.

# 5. Modelling of erosion and deposition pattern in standard divertor configuration

## 5.1. Plasma-background simulation in standard divertor configuration with EMC3-EIRENE

The experimental results presented before have been interpretatively modelled with the 3D PSI and transport code ERO2.0 [14] and the PSI code WallDYN-3D [15]. Mandatory input for both PSI codes is a 3D plasma background providing the key information about the plasma conditions in a divertor module and at the target plates: electron density  $n_{\rm e}$ , electron temperature  $T_{\rm e}$ , the ion temperature  $T_{\rm i}$ , the impinging ion flux  $\Gamma_{\rm i}$ , and the heat flux  $\Gamma_{\rm h}$ . The 3D Monte-Carlo Code EMC3-EIRENE is the most suitable plasma boundary code to provide these information in the complex W7-X geometry [16]. EMC3-EIRENE is currently applied to simulate the variety of experimentally accessible divertor plasma conditions in the standard divertor configuration of W7-X [17, 46] which offers the best set of experimental data to compare with. In order to interpret the

post-mortem analysis information on the horizontal and vertical target plates at the low  $\iota$  part of the TDU, in principle a selection of the most relevant magnetic configurations and representative plasma conditions is required to mimic the integrated conditions of one experimental campaign. As discussed before, the plasma-surface interaction zones are determined by the selected magnetic configuration and operational time, the footprints of configurations are well separated in space, and the configurations have in first order assumption negligible impact on each other. The initial plasma boundary modelling studies target on hydrogen plasmas with low O content (<0.1%) as present in OP1.2B.

A representative plasma background from EMC3-EIRENE in standard magnetic configuration with ionising divertor conditions in H was selected from experimental and modelling studies described in [47]. The target plasma used an upstream density of  $4 \times 10^{19}$  m<sup>-3</sup>, an input power of 4.0 MW, a radiated power fraction of 33% modulated by moderate impurity seeding, and a down stream peak heat flux at the strike line of

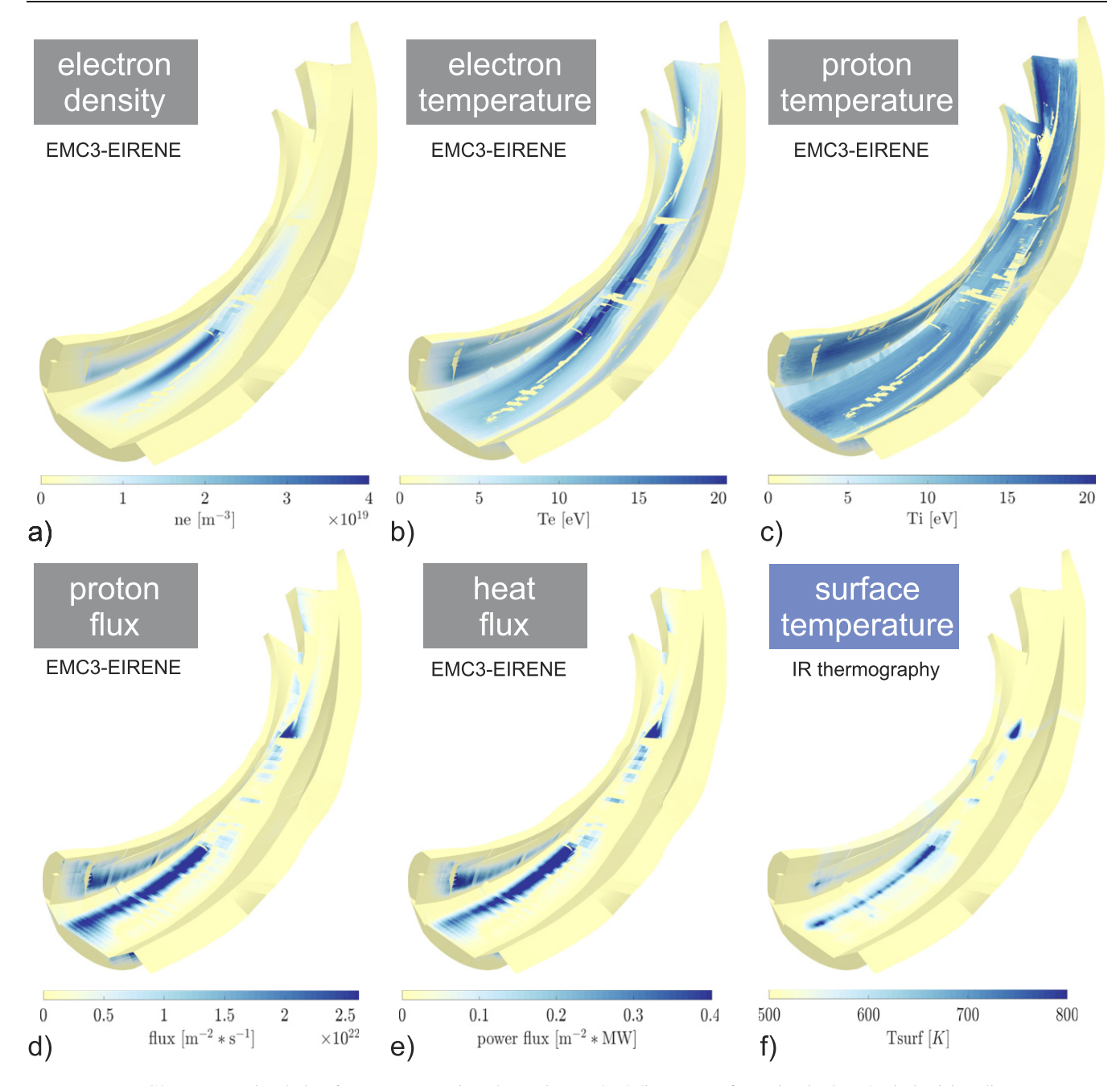


**Figure 14.** EMC3-EIRENE simulation for a representative plasma in standard divertor configuration in OP1.2B in ionising divertor conditions. (a)–(e) the main output parameter for PSI modelling:  $n_e$ ,  $T_e$ ,  $T_i$ ,  $\Gamma_i$ , and  $\Gamma_h$ . (f) The surface temperature distribution from the reference experiment measured by IR thermography.

1.0 MW m<sup>-2</sup>. The latter has been extensively compared with experimental heat fluxes at the divertor target plates. Figure 14 provides the set of relevant EMC3-EIRENE output parameters for the PSI modelling related to one divertor half module. The edge plasma of 1/10 of W7-X, representing one divertor half module, was simulated with the horizontal and vertical target plates as main material boundary; other PFCs like the first wall steel panels or the graphite heat shield have been neglected. Periodic boundary conditions and top-down symmetry was assumed.

The very same target plasma was applied in the  $^{13}$ CH<sub>4</sub> injection experiment at the end of plasma operation with TDU before removal of all divertor PFCs [48]. About 7% of plasma time in standard divertor configuration in OP1.2B was carried out in a sequence of self similar plasmas with divertor target plasma conditions of  $T_{\rm e}=25$  eV and  $1.0\times10^{19}$  m<sup>-3</sup> at the strike line on the HT. The EMC3-EIRENE plasma background was compared with plasma parameters from divertor Langmuir probes, IR thermography, and He beam and was in good agreement as described in more detail in [49]. Thus, the

selected EMC3-EIRENE plasma background is most suitable and representative for the adjacent PSI modelling studies with ERO2.0 and WallDYN-3D.

## 5.2. Simulations of C erosion and deposition on the TDU divertor target plates with ERO2.0

The 3D impurity transport and PSI code ERO2.0 has been applied to model the campaign integrated C erosion and deposition in W7-X equipped with graphite test divertor unit. ERO2.0 is a parallelised Monte-Carlo code operating on high performance computer and capable to simulate PSI processes (erosion, deposition, material mixing etc) and impurity transport with full gyro-orbit resolution in the boundary layer of large scale fusion plasmas devices like ITER [14] with high spatial resolution at the PSI. ERO2.0 applies the trace particle approximation for the impurities, thus the impact of traced impurities on the plasma background is neglected. The plasma and neutral particle background up to the main PFCs in the complex 3D geometry of W7-X is taken from EMC3-EIRENE. As in the case of EMC3-EIRENE, full five-fold symmetry of the W7-X modules and top/down symmetry within a module is assumed in ERO2.0 in the simulations regarding campaign-integrated material migration. One half module, or 1/10 of the plasma boundary and divertor PFCs is simulated with appropriate boundary conditions to ensure particle conservation.

ERO considers chemical and physical sputtering of carbon by impinging protons, carbon ions, and charge-exchange hydrogen with sputtering yields based on binary collision approximations according TRIM.SP [50]. Chemical sputtering is embedded following the Roth parametrisation [51] and the complete hydrocarbon break-up chain in the plasma [52] as well as sticking coefficients for hydrocarbon break-up products are considered. Though in the applied ERO2.0 version polished plasma-facing surfaces are considered, an effective impact angle of projectiles of 40° to surface normal was used to mimic the impact of roughness effects. This factors in the deviation from the typical mean impact angle of 60° observed in many ERO simulations with flat surface. WallDYN applies the same impact angle as discussed in [49]. A more realistic material roughness description [53] can be taken into account in future simulations on cost of calculation time. ERO2.0 can be compared in two ways with experimental results: (i) spectroscopy and experimental light emission of impurities eroded, ionised, excited in the plasma background; (ii) post-mortem analysis and the net erosion and deposition pattern. The focus in the campaign integrated study is on the simulation of the 2D distribution of net C erosion and deposition on the graphite PFCs of the TDU in high spatial resolution which permits a direct comparison with post-mortem analysis results presented in section 4.

Applying the EMC3-EIRENE plasma background for the standard divertor configuration (section 5.1), ERO2.0 simulates the gross erosion flux pattern of C from the divertor half module as depicted in figure 15(a) which considers the different erosion mechanisms described before. O has not been considered in these ERO2.0 simulations as the focus of the

present studies is on OP1.2B with negligible O content after application of the boronisations. Major correlation with the impinging ion and heat flux footprint at the strike-line location shown in figures 14(d) and (e) can be seen, but additional erosion related to the surface temperature footprint, thus, the chemical erosion can be identified. In general, the gross C erosion pattern reflects a combination of all three contributions. Figure 15(b) shows correspondingly the total deposition flux of C onto the divertor half module. The total deposition flux follows largely the impinging particle flux pattern and therefore, the gross C erosion and total C deposition footprint in distribution and magnitude look similar. The balance of both fluxes (figure 15(c)) provides the key result from the ERO2.0 simulations to be compared with the experiment, the net C erosion and deposition distribution along the plasma-facing surfaces of the TDU half module.

Figure 16(a) reassembles enlarged the key outcome of ERO2.0 simulations for the standard divertor configuration in W7-X hydrogen plasmas in OP12.B: the net C erosion and deposition flux pattern in one half module. The position of the marker target elements TM2h6 on the horizontal target plate and TM2v2 on the vertical target element are marked in the figure. In the next step the net C erosion and deposition flux pattern at the locations of the target modules is integrated in a small stripe in toroidal direction in order to improve the simulation statistics. Figure 16(b) depicts the profile of simulated net C erosion and deposition flux along the poloidal coordinate s at the toroidal location of TM2h6 on the horizontal target element. The profile reproduces qualitatively well the main features observed in the experimental analysis shown in figure 9(c) for the averaged profile over all HMs: the strong and broad erosion region at the location of the inner strike-line, a moderate deposition region in the area of the magnetic island, followed by second moderate erosion zone related to the outer strike-line, finally a zone of balanced erosion and deposition at the end of the target element. Multiplication with the experimental time in standard divertor configuration in OP1.2B provides the integrated net eroded and deposited C at this location. The simulated peak erosion values are in good agreement in the absolute magnitude with the experiment. However, ERO2.0 predicts a significant net-erosion between the PG and the inner strike line on the HT which cannot be seen in the experiment. A potential cause might be the overestimation of chemical erosion in ERO2.0 at this location as the comparison of figures 16(d) and (e) suggests. In future simulations the more recent description of the chemical erosion yield with ion flux dependence [54] will be applied.

Figure 16(c) shows the corresponding ERO2.0 net C erosion and deposition flux distribution along the poloidal coordinate s at the toroidal position of TM2v2. The simulation predicts rightfully the peak net erosion close to the strike-line position of the vertical target. However, the extension of the net erosion zone is wider and no deposition area close to the baffle region is visible as seen in the experiment e.g. in figure 13(c) for the lower half module 5 (HM 51). The main contributor to the broad erosion on the VT plate in ERO2.0 is chemical sputtering which seems to be overestimated in comparison with the experimental results. Moreover, there is a discrepancy by about

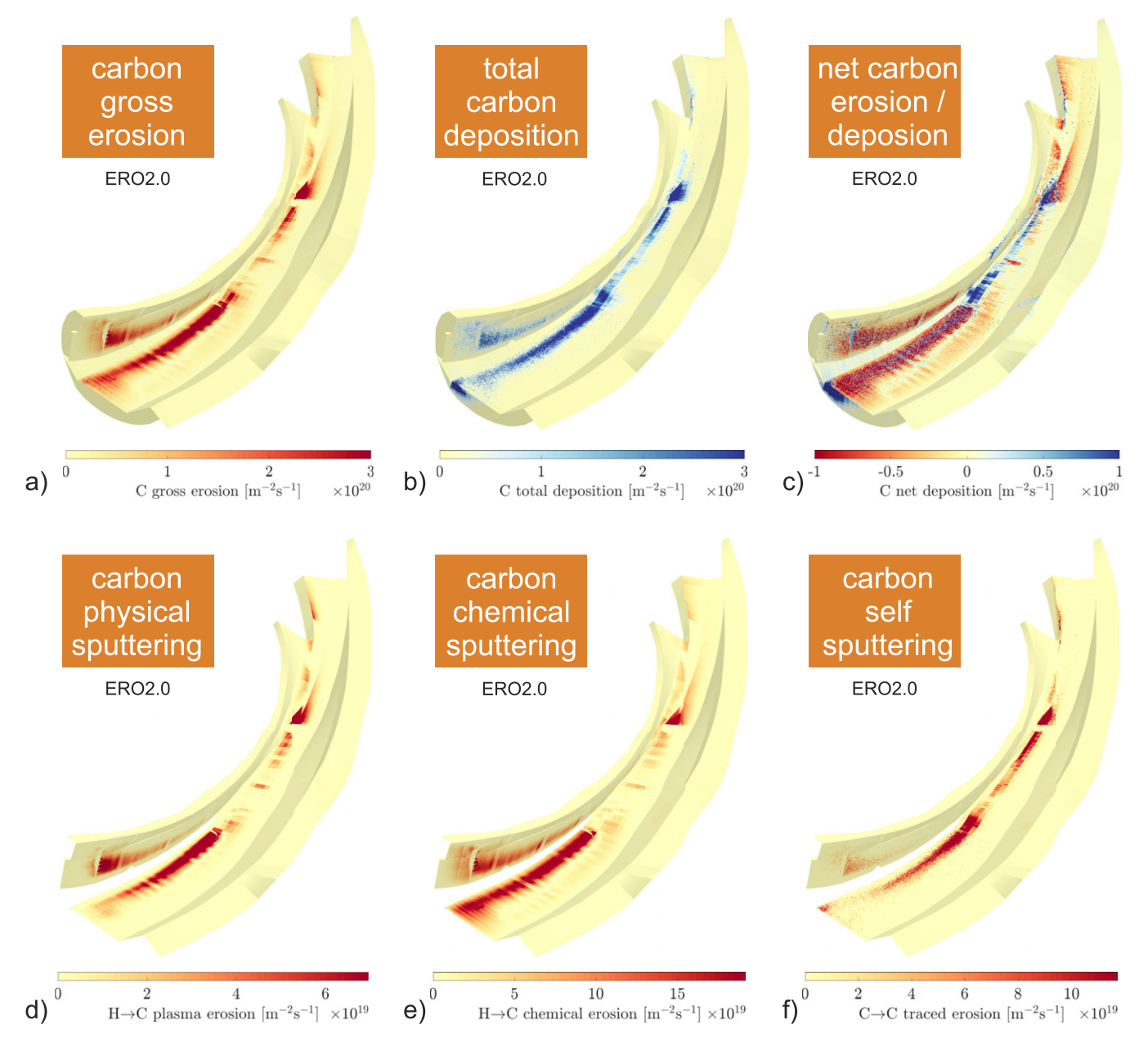


**Figure 15.** ERO2.0 simulations of C erosion and deposition at one graphite half module exposed in W7-X hydrogen plasmas in standard divertor configuration. (*a*) Gross C erosion distribution on the divertor target plates. (*b*) Total C deposition distribution on the divertor target plates. (*c*) The net C erosion and deposition pattern on the divertor plates. (*d*) Physical sputtering of graphite by protons. (*e*) Chemical sputtering of graphite by protons. (*f*) Self-sputtering of graphite by C ions.

a factor 3 in the magnitude of peak net C erosion between modelling and experimental results from HM 51 when normalising to the operational time in OP1.2B. It shall be noted, that due to lack of analysis, no averaged profile over the ten HMs exist and HM 51 showed 40% more peak erosion that HM 5u. Thus, the discrepancy between ERO2.0 simulation and an averaged net C erosion and deposition is expected to be lower, but will still be significant. The high mirror configuration (KJM) might contribute at this location to additional C erosion as discussed in the experimental section 4.3.

The main experimental features like the two erosion zones due to strike lines, the deposition in-between them, and the peak net C erosion can be quantitatively well reproduced for the HT plate by ERO2.0 for the standard divertor configuration with graphite PFCs. Therefore, ERO2.0 can be applied for predictive modelling of erosion/deposition in OP2.0 with actively cooled divertor provided a relevant plasma background for long-pulse operation is available. Differences between experiment and interpretative modelling of the VT plate appear. On the one hand the peak net C erosion location is reproduced, but the modelled net erosion is too low. On the other hand, ERO2.0 failed to predict the deposition zone close to the baffle at the inboard side which is likely related to an overestimation of the chemical erosion contribution. ERO2.0 simulations at this stage are not considering further interaction at e.g. the inner heat shield made of graphite or other recessed plasma-

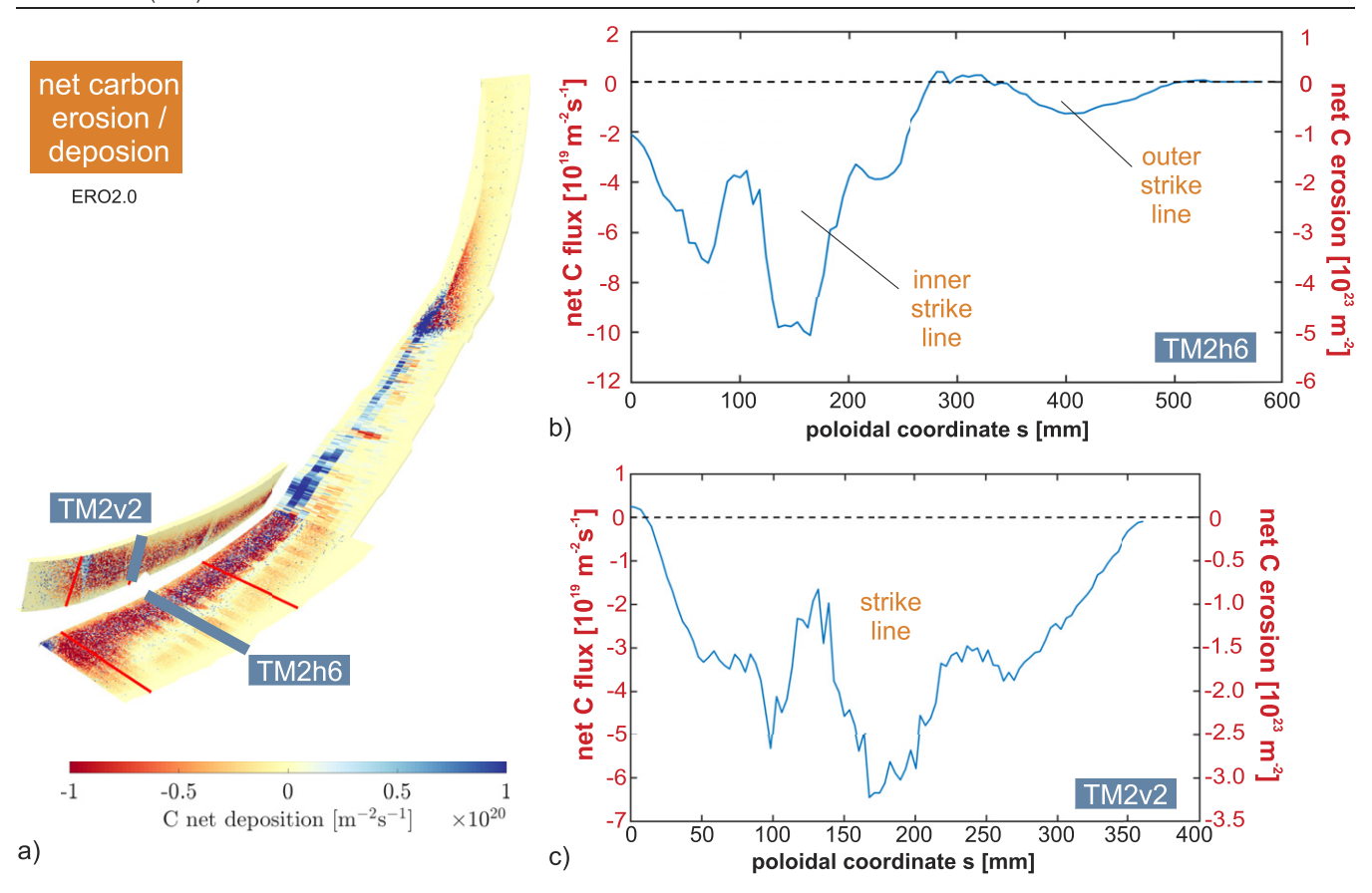


**Figure 16.** ERO2.0 simulation of the net C erosion and deposition distribution on the HT and VT plates in standard divertor configuration. (*b*) Horizontal target: poloidal distribution of the net C erosion and deposition flux at the toroidal location TM2h6. Integrated net C erosion and deposition in OP1.2B. (*c*) Vertical target: poloidal distribution of the net C erosion and deposition flux at the toroidal location TM2v2. Integrated net C erosion and deposition in OP1.2B.

material surface. Inclusion of these areas might improve the overall global simulations and support the estimation of an overall carbon balance. However, the required plasma conditions at those locations, namely the proton flux and the charge exchange hydrogen flux to those surface were not available at the time of the modelling. They will be included in future and permit simulations with PSI at all graphite bases surfaces. It shall be further mentioned that only one magnetic configuration with one experimental condition has been used up to now to model the complete net C erosion and deposition pattern after OP1.2B. ERO2.0 modelling of a representative high mirror configuration (KJM) plasma is required to improve the description of the net C erosion and deposition footprint on the vertical target. However, also here is the prerequisite representative EMC3-EIRENE plasma background solution as input currently not available.

# 5.3. The $^{13}\text{CH}_4$ injection experiment in W7-X and its interpretative modelling

The <sup>13</sup>CH<sub>4</sub> injection permits the study of C transport and global C migration in the all-C W7-X utilising both carbon spectroscopy and post-mortem analysis on graphite PFCs. The first <sup>13</sup>C marker experiment has been carried out as last experiment before the complete extraction of all PFCs of the

test divertor unit. The experimental target plasmas was, as described before, a representative hydrogen plasma for the campaign OP1.2B (core electron temperature  $T_{\rm e}^{\rm C}=(2.8-3.2)$  keV, core electron density  $n_{\rm e}^{\rm C}=(5.0-6.0)\times10^{19}$  m<sup>-3</sup>, ECR heating power  $P_{\rm ECRH}=(3.4-3.9)$  MW) with attached divertor conditions, thus, with clear heat and particle flux footprints which can be correlated to the <sup>13</sup>C footprints representing the C transport in W7-X. The divertor plasma conditions are described in detail in section 5.1 and [49].

In order to deposit detectable levels of <sup>13</sup>C on the graphite PFCs, multiple consecutive repeats of almost identical discharges were done accumulating 330 s of plasma time with  $^{13}\text{CH}_4$  injection. In total  $4.5 \times 10^{22}$   $^{13}\text{C}$  atoms were introduced as <sup>13</sup>CH<sub>4</sub> molecules through two point-like gas inlets located in HM 31 close to the O-point of the magnetic island intersecting the HT plate [48, 55]. The injected C isotope <sup>13</sup>C mimics the erosion source of natural <sup>12</sup>C at the HT plate and allows to follow-up C transport paths in W7-X. After extraction of the all TDU PFCs from the vessel, nuclear reaction analysis is applied in order to determine the <sup>13</sup>C distribution on the horizontal and vertical plates including (i) marker target elements [39] and (ii) standard TDU fingers made of fine grain graphite [56]. The post-mortem analysis is not yet fully completed, but first information can be given at this stage and compared with WallDYN-3D modelling results [49].

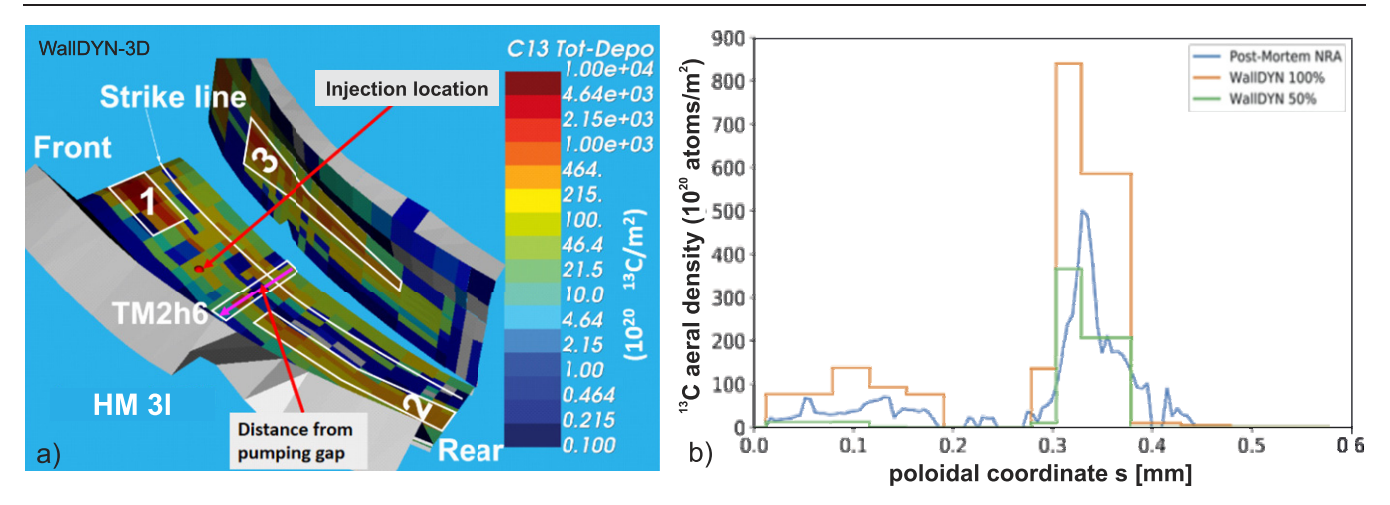


**Figure 17.** WallDYN-3D simulation of  $^{13}$ C injection into a magnetic island in the standard divertor configuration through HM 3l . (a) Net  $^{13}$ C deposition distribution on the target plates. Reproduced from [49]. CC BY 4.0. (b) Measured and modelled  $^{13}$ C areal density in poloidal direction at the location of TM2h6. The fraction of  $^{13}$ C particles escaping from the half module was varied between zero and 50% corresponding to the WallDYN results with the labels 100% and 50%. Reproduced from [49]. CC BY 4.0.

WallDYN-3D coupled to EMC3-EIRENE simulates the full W7-X torus by mirroring multiple times the geometry and plasma background of one HM with appropriate periodic boundary conditions providing a fully symmetric environment of all five modules. The full symmetry assumption for the background plasmas and the PSI processes is broken by the toroidally localised marker gas injection through a point-like gas source in the model located in the horizontal target plate of the lower half module 3 lower (HM 31). WallDYN-3D introduces in a simplified manner directly <sup>13</sup>C atoms instead of <sup>13</sup>CH<sub>4</sub> molecules into the plasma and the <sup>13</sup>C transport in the torus is followed in the simulation. Subsequently, the deposition of <sup>13</sup>C on the considered wall surfaces of the model is determined via a transport matrix, providing the net <sup>13</sup>C deposition pattern for the integrated plasma time of the marker injection experiment. Local perturbations of the plasma background at the location of the <sup>13</sup>C injection are not taken into account, but the EMC3-EIRENE plasma background considers a steady-state plasma with effective moderate methane seeding. The key results of the interpretative WallDYN-3D modelling of the <sup>13</sup>C injection from the horizontal target plate in W7-X are depicted in figure 17. Dominant local <sup>13</sup>C deposition in the very same half module 3 lower (HM 31) occurs up and down stream of the injection location marked as areas 1 and 2. Local deposition of the isotopically marked <sup>13</sup>C occurs also on the VT plate labelled as area 3 in figure 17(a). In addition, deposition of  $^{13}$ C takes place close to the dominant strike-line location of the standard divertor configuration on the HT, where re-distribution of deposited <sup>13</sup>C by re-erosion of both <sup>12</sup>C and <sup>13</sup>C takes place. Figure 17(b) provides a quantitative comparison of simulation and experiment with respect to the areal density of deposited <sup>13</sup>C at the toroidal location of the marker target element TM2h6 in the injection half module 31. Dedicated postmortem analysis utilising ion beam technique was applied on top of the previously discussed EBS studies focussing on <sup>12</sup>C (section 4) in order to quantify <sup>13</sup>C at the top surface [39].

The WallDYN-3D simulation reproduces well the <sup>13</sup>C deposition pattern on the target element TM2h6 in poloidal direction: a strong localised deposition zone around the poloidal coordinate of the injection location and a weaker, smeared deposition zone next to the strike-line location. The agreement in absolute magnitude is satisfying; the experimental values lay between two assumptions about the fraction of <sup>13</sup>C remaining in steady-state conditions in the half module (50% or 100%) where the injection took place. Further details about the interpretative WallDYN-3D modelling and the overall benchmark of the first tracer experiment in W7-X are given in [49].

These first studies are complemented by ERO2.0 simulations which include the injection of <sup>13</sup>CH<sub>4</sub> molecules, their break-up in the plasma, and sticking of <sup>13</sup>CH<sub>v</sub> fragments on surfaces of the injection half module 31 as well as the distribution in the full W7-X vessel [55]. ERO2.0 simulates in this case of asymmetric impurity injection the full W7-X vessel with all half modules. In contrast to WallDYN-3D, the followup of <sup>13</sup>CH<sub>v</sub> fragments enhances the local <sup>13</sup>C deposition close to the injection location as the penetration of the molecules is limited as seen in other ERO studies in tokamaks before [57]. ERO2.0 detects 44.5% of the injected <sup>13</sup>C within a radius of 5 cm around the injection location close to the O-point of the intersecting island. Overall 82% of the introduced <sup>13</sup>C remain in half module 31 were the <sup>13</sup>CH<sub>4</sub> was introduced into the divertor plasma [55]. The overall deposition locations are comparable to the WallDYN-3D observations as well as the fraction of <sup>13</sup>C leaving the HM are in fair agreement. In the next step ERO2.0 will follow the multiple erosion/deposition process cycle and give an insight on the stepwise migration of <sup>13</sup>C in the W7-X vessel.

#### 6. Summary and conclusion

The plasma operation with the graphite TDU provided vital information about the operational window and PSI processes

in W7-X operating with island divertor. No significant damage occurred to the inertially cooled PFCs in the two temporally separated campaigns OP1.2A and OP1.2B with an integral plasma operation time of 3.6 h in hydrogen and helium. The operational window, restricted in OP1.2A due to high oxygen and carbon content in the plasma owing to water contamination in the PFCs, opened up with the application of boronisations. Boronisation gettered oxygen in boron layers, reduced dramatically the carbon erosion at the PFCs, and permitted, at reduced impurity content in the plasma, the access to the stellarator-favoured high density operation in the core and functional divertor operation with high neutral compression [58]. These optimised first wall conditions are a prerequisite for the foreseen long-pulse operation in W7-X with the new actively cooled divertor [7] aiming at hydrogen plasmas of 1800 s pulse duration. The 3D shape of the inertially cooled graphite divertor and the actively cooled carbon-fibre composite (CFC) divertor is identical and follows the plasma contour in W7-X. Extrapolation of plasma exhaust and PSI processes, which includes the impurity source strength estimation, potential carbon dust formation, and the associated lifetime prediction of divertor PFCs, towards long pulse operation with the actively cooled island divertor is therefore most relevant and reliable when either (a) based directly on experimental results obtained in operational phase 1.2B or (b) based on simulations of plasma exhaust and PSIs with codes like EMC3-EIRENE, ERO2.0, and WallDYN-3D validated on W7-X OP1.2B experiments. The inertially cooled graphite PFCs of the TDU received peak heat loads up to 10 MW m<sup>-2</sup> at the high heat flux zones of the HT plate and VT plate covering a total area of 19 m<sup>2</sup> of which typically only one 1/10 is wetted by the ionising plasma in the different applicable magnetic configurations explored so far in W7-X. The corresponding particle loads with peak fluxes up to few  $10^{23}$  ions s<sup>-1</sup> m<sup>-2</sup> at the strike lines under attached divertor conditions resulted in a manifold of PSI processes related to carbon erosion, transport, deposition and hydrogen retention by implantation and co-deposition with carbon. Carbon erosion follows—as demonstrated in the case of the standard magnetic divertor configuration—the heat and particle footprint on the divertor target plates resulting in strong net erosion zones at the strike lines and local deposition away from those e.g. close to the O-point of an magnetic island. Interpretative ERO2.0 modelling reproduced, in particular also quantitatively on the horizontal target plate, the measured erosion/deposition pattern in OP1.2B and its relation to ionising plasma conditions in the standard divertor configuration. In contrast to tokamak applications with large variations in divertor configurations and plasma shapes, in the case of W7-X the integrated campaign pattern can in the first order be separated into a small set of basic magnetic configurations as the heat and particle footprint is within this configurations to a large extend separated on the target plates of the TDU. The shadowed or unexposed areas in those configuration can in first order approximation be treated as recessed areas. Correlation between the configuration and the measured integrated net carbon erosion and deposition can be done under consideration of the operational time in the configuration. The next step of analysis requires the inclusion of recessed first wall components on the carbon migration cycle in W7-X. This must include in particular the erosion of e.g. graphite PFCs of the heat shield by protons and charge-exchange hydrogen atoms as well as deposition of once eroded carbon on those PFCs in a given magnetic divertor configuration. This more detailed study will feed into an overall carbon balance in W7-X for OP1.2B, but is out of the scope of the present studies. At this stage we can only refer to recent campaign-integrated information from colorimetric and marker sample analysis after OP1.2B [60] indicating after introduction of boronisations, that the first wall is to a large extent in erosion/deposition balance or shows in specific, mostly shadowed regions, deposition [59, 67]. This is inline with the conclusion of the campaignintegrated analysis presented here: the TDU is a net C erosion source.

The standard divertor configuration is the best characterised magnetic configuration from PSI perspective in W7-X and it was executed for the majority of operational time in OP1.2B (53%). The footprint of net C erosion/deposition of PFCs and H content in PFCs has been assessed in the standard divertor configuration via two main paths (a) campaign integrated post-mortem analysis of PFCs utilising in particular marker target elements, and (b) a <sup>13</sup>CH<sub>4</sub> injection as last experiment of OP1.2B accumulating 330 s of similar plasma conditions. Operation in attached divertor conditions was dominant in OP1.2B and caused, despite O concentrations below 0.1\%, peak net C erosion about 10  $\mu$ m at the strike line on the VT plates, which is equivalent to 2.5 nm s<sup>-1</sup> of C erosion by protons and C ions. Considering the total number of half modules, this amounts to a campaign integrated net C erosion of (6.8 + / - 1.2) g C. The corresponding analysis of the HT plate revealed a campaign integrated net C erosion of (13.7 + / - 2.3) g C in OP1.2B or net C erosion rates of  $(2.8 + /0.5) \text{ mg s}^{-1}$  when related to 4809 s of plasma time in standard configuration in H. The integrated net C erosion at the HT and VT plates of the inertially cooled TDU corresponds to  $\simeq 2.5$  long-pulse discharges of 1800 s duration under typical attached and ionising divertor plasma conditions operated in standard magnetic divertor configuration in OP1.2B. The predicted net C erosion source in the divertor would amount 7.6 g C per 1800 s discharge if similar plasma and divertor conditions as in OP1.2B would be applied in the next operational phase of W7-X with actively cooled CFC divertor. We shall stress, that the predictions are made under the assumption of symmetric particle and power loads onto the ten divertor half modules. Moderate deviations from this symmetry assumption have been observed and related to alignment uncertainties with the TDU (half module to half module) as well as to physicsdriven causes (top to down) by particle flows. This poses an uncertainty in particular on the peak-erosion rates and the surface temperature footprint in absolute numbers. The latter impacts on the source strength of chemical erosion of graphite which is temperature dependent. However, the predicted net C erosion source per 1800 s based on the symmetric assumptions can be applied as good and best as available guidance to the operation in OP2. The total C erosion per pulse as

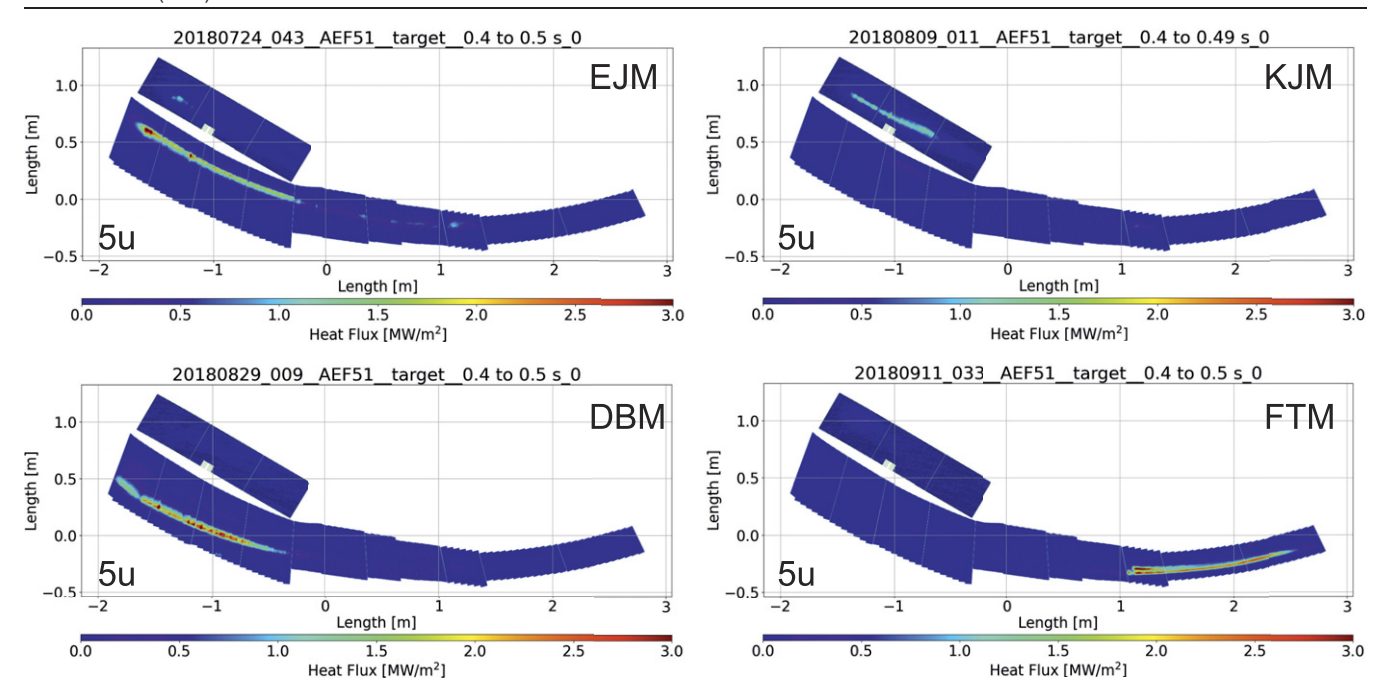


**Figure 18.** IR thermography footprint of main magnetic divertor configurations used in W7-X during OP1.2B. Measurements were taken in hydrogen plasma under ionisation conditions in half module 5u (HM 5u). The IR data was averaged between t = 0.4 s to 0.5 s after start of the plasma start in the corresponding configuration. The corresponding input power amount (i) EJM: 2.7 MW, (ii) DBM: 3.8 MW, (iii) KJM: 2.1 MW, and (iv) FTM: 3.8 MW Details about the applied IR system and the interpretation of experimental data can be found in [8,71].

well as the peak C erosion could hamper plasma operation with time in OP2 causing C dust production from unstable C layers in deposition zones. Tore Supra [61] and LHD [62], both equipped with actively cooled graphite-based PFCs, had experienced the multistep C erosion/deposition cycle with the release of C clusters or C dust particles from disintegrated layers which impacted strongly steady-stare plasma operation. Such type of C dust would have a very critical impact on the duty cycle and the safety of a reactor-like stellarator with graphite components if divertor conditions like in OP1.2B would be applied.

Potential counter measures required for reliable and safe long pulse operation in W7-X are (a) reduction of the C source by operation with cold, detached divertor [63], (b) optimised wall conditioning techniques to avoid carbon layer formation with high fuel content [64], and (c) ultimately change of the PFC material to e.g. tungsten [65]. The use of W as plasmafacing material in W7-X [66, 67] requires besides the PSI and lifetime aspects of components additionally the compatibility with plasma operation and performance, thus, e.g. the avoidance of W accumulation. The transfer from an all-C W7-X to a metallic facility faces similar challenges as mastered in the tokamaks ASDEX Upgrade [68], WEST [69], and JET [70]. It shall be again stressed, that the presented pure experimental extrapolation to long pulse operation is based on one typical (average) plasma and variations exist depending on the actual plasma boundary conditions and divertor regime which have been explored in OP1.2B.

Interpretative ERO2.0 and WallDYN-3D modelling of such a typical W7-X plasma with attached and ionising divertor conditions reproduced the observed net C erosion/deposition

pattern as well as revealed C migration paths in the standard divertor configuration. The exact 2D erosion and deposition pattern on the target plates is complex due to the 3D shape of the TDU which follows the five-fold island divertor structure present in W7-X. Interpretative modelling requires therefore in all cases a full 3D treatment in contrast to tokamaks where axial symmetry can often be assumed. Reduction of the plasma simulation volume and the plasmafacing surfaces to 1/10, or one divertor HM, can be applied assuming perfect fivefold symmetry as well as top/down symmetry. Deviations from the symmetry assumption, observed in experiments, cannot be treated with a symmetric plasma boundary background. This uncertainty for attached divertor conditions needs to be taken into account in predictions for long-pulse operation. Note that detached divertor operation shows in experiments symmetric particle and heat loads to all HMs and minimises the modelling uncertainties with this respect [71].

Further interpretative modelling of other magnetic configurations used in OP1.2B like e.g. the high mirror (KJM) or low iota configuration (FTM) with EMC3-EIRENE and ERO2.0 are foreseen in future. The simulation information about net C erosion and deposition will be compared with post-mortem analysis on representative target fingers of those configurations. The simulations will help to explore the capability of these configurations for long pulse operation from the PSI and plasma exhaust perspective. Moreover, the range of ERO2.0 simulations in standard divertor configuration will be expanded to plasmas with impurity seeding (Ne or N<sub>2</sub>) and detached divertor conditions [46, 71] once suitable EMC3-EIRENE simulations are available. Impurity seeded plasmas

**Table 1.** Overview of main configuration families in OP1.2A: plasma species, operational time, and fraction of operational time. Though only 28% of plasma discharges were associated with pure  $H_2$  injection into W7-X, the plasma operation took predominantly place in H + He plasmas due to outgassing of  $H_2$  from the vessel walls.

OP1.2A: Configuration family	Species	Plasma time (s)	Fraction (%)
Standard divertor Configuration (EJM)	H + He	2481	65.6
High mirror Configuration (KJM)	H + He	714	18.9
High iota Configuration (FTM)	H + He	434	11.5
Diverse	H + He	147	3.9
Total	H + He	3776	99.9

**Table 2.** Overview of main configuration families in OP1.2B: plasma species, operational time, and fraction of operational time. Note minor operation in He took place before the first boronisation.

Configuration family	Species	Plasma time (s)	Fraction (%)
Standard divertor Configuration (EJM)	Н	4809	53.1
High mirror Configuration (KJM)	Н	1392	15.3
Low iota Configuration (DBM)	Н	1180	13.0
High iota Configuration (FTM)	Н	1673	18.5
Total	Н	9054	99.9

are one of the most promising candidates to comply with the power load restriction to the target plates with enlarged input power in W7-X. Moreover, they are attractive from the standpoint of carbon erosion. Finally, predictive modelling of long pulse discharges with actively cooled CFC divertor and first wall components will be carried out soon with the aim to provide an insight of the C balance in targeted 1800 s long discharges with island divertor as well as compatibilities of such discharges with an all-W divertor in W7-X.

#### **Acknowledgments**

This work has been carried out within the framework of the EUROfusion Consortium and has received funding from the Euratom research and training programme 2014–2018 and 2019–2020 under grant agreement No. 633053. The views and opinions expressed herein do not necessarily reflect those of the European Commission. This work is supported by DFG Grant No. 410415657. The authors gratefully acknowledge the computing time granted through JARA on the supercomputer JURECA [72] at Forschungszentrum Jülich. This work was supported by the United States Department of Energy (DoE) under Grants No. DE-AC02-09CH11466, and DE-SC0014210. The authors thank Torsten Bräuer for the provision of images taken in the vessel of W7-X after OP1.2B.

# Appendix A. Magnetic divertor configurations and their operational times

A.1. Heat load footprints

See figure 18.

A.2. Campaign statistics

See tables 1 and 2.

#### **ORCID iDs**

S. Brezinsek https://orcid.org/0000-0002-7213-3326 M. Jakubowski https://orcid.org/0000-0002-6557-3497 R. König https://orcid.org/0000-0002-4772-0051 S. Masuzaki https://orcid.org/0000-0003-0161-0938 M. Mayer https://orcid.org/0000-0002-5337-6963 D. Naujoks https://orcid.org/0000-0003-4265-6078 J. Romazanov https://orcid.org/0000-0001-9439-786X O. Schmitz https://orcid.org/0000-0002-9580-9149 D. Zhao https://orcid.org/0000-0003-0387-4961 M. Balden https://orcid.org/0000-0002-8755-9370 B. Butterschoen b https://orcid.org/0000-0002-9830-9641 T. Dittmar https://orcid.org/0000-0002-4325-7979 P. Drews https://orcid.org/0000-0002-6567-1601 F. Effenberg https://orcid.org/0000-0002-4846-4598 O. Ford https://orcid.org/0000-0002-5646-4758 E. Fortuna-Zalesna https://orcid.org/0000-0002-1090-1641 G. Fuchert https://orcid.org/0000-0002-6640-2139 Y. Gao https://orcid.org/0000-0001-8576-0970 A. Goriaev https://orcid.org/0000-0002-2599-182X A. Hakola https://orcid.org/0000-0003-1385-1296 T. Kremeyer https://orcid.org/0000-0002-6383-944X Y. Liang https://orcid.org/0000-0002-9483-6911 Ch. Linsmeier https://orcid.org/0000-0003-0404-7191 R. Lunsford https://orcid.org/0000-0003-3588-6801

G. Motojima https://orcid.org/0000-0001-5522-3082

J. Oelmann https://orcid.org/0000-0002-0845-4571

R. Neu https://orcid.org/0000-0002-6062-1955
O. Neubauer https://orcid.org/0000-0002-4516-4397

- M. Rasinski https://orcid.org/0000-0001-6277-4421
- M. Rubel https://orcid.org/0000-0001-9901-6296
- S. Sereda https://orcid.org/0000-0003-0180-6279
- G. Sergienko https://orcid.org/0000-0002-1539-4909
- T. Sunn Pedersen https://orcid.org/0000-0002-9720-1276
- T. Vuoriheimo https://orcid.org/0000-0003-4266-9178
- T. Wauters https://orcid.org/0000-0002-2941-7817
- V. Winters https://orcid.org/0000-0001-8108-7774
- M. Zhao b https://orcid.org/0000-0001-5089-3642
- R. Yi https://orcid.org/0000-0002-4422-5178

#### References

- [1] Klinger T. et al 2019 Nucl. Fusion 59 112004
- [2] Fujiwara M. et al 1998 Plasma Fusion Res. Series 1 52 (http://www.jspf.or.jp/JPFRS/PDF/Vol1/jpfrs1998\_01-057.pdf)
- [3] Sunn Pedersen T. et al 2019 Nucl. Fusion 59 096014
- [4] Peacock A. et al 2011 Fusion Eng. Des. 86 527
- [5] König R. et al 2021 24th International Conference on Plasma Surface Interactions in Controlled Fusion Devices PSI Conf. (Jeju Island, South Korea, 24–29 January 2021)
- [6] Fuchert G. et al 2020 Nucl. Fusion 60 036020
- [7] Boscary J., Peacock A., Stadler R., Mendelevitch B., Tittes H., Tretter J., Smirnow M. and Li C. 2013 Fusion Sci. Technol. 64 263
- [8] Gao Y., Jakubowski M.W., Drewelow P., Pisano F., Puig Sitjes A., Niemann H., Ali A. and Cannas B. 2019 Nucl. Fusion 59 066007
- [9] Dhard C.P. et al 2019 Fusion Eng. Des. 146 242
- [10] Sereda S. et al 2020 Nucl. Fusion 60 086007
- [11] Mayer M. et al 2020 Phys. Scr. **T171** 014035
- [12] Zhao D. 2020 Phys. Scr. T171 014018
- [13] Mayer M. et al 2002 Nucl. Instrum. Methods Phys. Res. B 194 177
- [14] Romazanov J. et al 2019 Nucl. Mater. Energy 18 331
- [15] Schmid K. et al 2018 Nucl. Mater. Energy 17 205
- [16] Feng Y. et al 2014 Contrib. Plasma Phys. 54 426
- [17] Effenberg F. et al 2019 Nucl. Mater. Energy 18 262
- [18] Hathiramani D. et al 2018 Fusion Eng. Design 136 304
- [19] Rudischhauser L., Endler M., Höfel U., Hammond K.C., Kallmeyer J.P. and Blackwell B.D. 2020 Rev. Sci. Instrum. 91 063505
- [20] Barbui T. et al 2019 J. Instrum. 14 C07014
- [21] Jakubowski M. et al 2018 Rev. Sci. Instrum. 89 10E116
- [22] Pedersen T.S. et al 2019 Plasma Phys. Control. Fusion 61 014035
- [23] Niemann H. et al 2020 Nucl. Fusion 60 084003
- [24] Dhard C.P. et al 2020 Phys. Scr. **T171** 014033
- [25] Motojima G., Masuzaki S., Dhard C.P., Krause M., Naujoks D., Hayashi Y. and Brezinsek S. 2020 Phys. Scr. T171 014054
- [26] Wienhold P. et al 1997 J. Nucl. Mater. 241-243 804
- [27] Ruset C., Grigore E., Munteanu I., Maier H., Greuner H., Hopf C., Phylipps V. and Matthews G. 2009 Fusion Eng. Des. 84 1662

- [28] Zhao D. et al 2021 Nucl. Fusion 61 016025
- [29] Wauters T. et al 2018 Nucl. Mater. Energy 17 235
- [30] Goriaev A. et al 2020 Phys. Scr. **T171** 014063
- [31] Wei Y. et al 2018 AIP Adv. 8 085011
- [32] Wei Y. et al 2019 Plasma Sci. Technol. 21 105102
- [33] Winter J. 1996 Plasma Phys. Control. Fusion 38 1503
- [34] Wang E. et al 2020 Phys. Scr. **T171** 014040
- [35] Butterschoen B 2020 (private communication)
- [36] Lunsford R. et al 2021 Phys. Plasmas 28 082506
- [37] Nagy A. et al 2019 Fusion Eng. Des. 146 1403
- [38] Eckstein W. et al 2007 Sputtering by Particle Bombardment, Topics in Applied Physics vol 110 (Berlin: Springer)
- [39] Mayer M. et al 2021 24th International Conference on Plasma Surface Interactions in Controlled Fusion Devices PSI Conf. (Jeju Island, South Korea, 24–29 January 2021)
- [40] Hammond K.C. et al 2019 Plasma Phys. Control. Fusion 61 125001
- [41] Oelmann J. et al 2021 Nucl. Mater. Energy 26 100943
- [42] Yi R. et al 2020 Appl. Surf. Sci. 532 147185
- [43] Roth J. et al 2009 J. Nucl. Mater. 390-391 20
- [44] Brezinsek S. et al 2007 J. Nucl. Mater. 363-365 1119
- [45] Zhao D. et al 2021 Phys. Scr. (in review)
- [46] Winters V.R. et al 2021 Plasma Phys. Control. Fusion 63 045016
- [47] Effenberg F. et al 2019 Nucl. Fusion 59 106020
- [48] Brezinsek S. et al 2019 17th International Conference on Plasma Facing Materials and Components PFMC Conf. (Eindhoven, Netherlands, 20–24 May 2019)
- [49] Schmid K. et al 2020 Nucl. Mater. Energy 25 10082
- [50] Mutzke A. et al 2019 IPP-Report 2019/2
- [51] Roth J. and Garcia-Rosales C. 1996 Nucl. Fusion **36**
- [52] Reiter D. and Janev R.K. 2010 Contrib. Plasma Phys. 50 986
- [53] Eksaeva A. et al 2019 Nucl. Mater. Energy 19 13
- [54] Roth J. et al 2005 J. Nucl. Mater. 337 970
- [55] Brezinsek S. et al 2021 PFMC conference Phys. Scr. (submitted)
- [56] Vuoriheimo T., Hakola A., Likonen J., Brezinsek S., Dittmar T., Mayer M., Prakash Dhard C., Naujoks D. and Tuomisto F. 2021 Phys. Scr. 96 124023
- [57] Kirschner A. et al 2013 J. Nucl. Mater. 438 S723
- [58] Schmitz O. et al 2021 Nucl. Fusion **61** 016026
- [59] Oelmann J. et al 2021 Phys. Scr.
- [60] Dhard C.P. et al 2021 Phys. Scr.
- [61] Tsitrone E. et al 2009 Nucl. Fusion **49** 075011
- [62] Tokitani M. et al 2015 J. Nucl. Mater. **463** 91
- [63] Brezinsek S. et al 2009 J. Nucl. Mater. **390–391** 267
- [64] Philipps V. et al 2005 Fusion Sci. Technol. 47 119
- [65] Philipps V. et al 2011 J. Nucl. Mater. 415 S2
- [66] Naujoks D 2020 (private communication)
- [67] Mayer M. et al 2021 Phys. Scr.
- [68] Neu R. et al 2013 J. Nucl. Materials 438 S34
- [69] Bourdelle C. et al 2015 Nucl. Fusion 55 063017
- [70] Brezinsek S. et al 2015 J. Nucl. Mater. 463 11
- [71] Jakubowski M. et al 2021 Nucl. Fusion 61 106003
- [72] Jülich Supercomputing Centre 2018 JURECA: Modular supercomputer at Jülich supercomputing centre J. Large-Scale Res. Facil. 4 A132